



HAL
open science

Role of the Early Miocene Jinhe-Qinghe Thrust Belt in the building of the Southeastern Tibetan Plateau topography

Chengyu Zhu, Guocan Wang, Philippe Hervé Leloup, Kai Cao, Gweltaz Mahéo, Yue Chen, Pan Zhang, Tianyi Shen, Guiling Wu, Paul Sotiriou, et al.

► **To cite this version:**

Chengyu Zhu, Guocan Wang, Philippe Hervé Leloup, Kai Cao, Gweltaz Mahéo, et al.. Role of the Early Miocene Jinhe-Qinghe Thrust Belt in the building of the Southeastern Tibetan Plateau topography. *Tectonophysics*, 2021, 811, 10.1016/j.tecto.2021.228871 . hal-03371256

HAL Id: hal-03371256

<https://univ-lyon1.hal.science/hal-03371256>

Submitted on 13 Oct 2021

HAL is a multi-disciplinary open access archive for the deposit and dissemination of scientific research documents, whether they are published or not. The documents may come from teaching and research institutions in France or abroad, or from public or private research centers.

L'archive ouverte pluridisciplinaire **HAL**, est destinée au dépôt et à la diffusion de documents scientifiques de niveau recherche, publiés ou non, émanant des établissements d'enseignement et de recherche français ou étrangers, des laboratoires publics ou privés.

1 **Role of the Early Miocene Jinhe-Qinghe Thrust Belt in the building of the**
2 **Southeastern Tibetan Plateau topography**

3
4 **Chengyu Zhu¹, Guocan Wang^{1,2}, Philippe Hervé Leloup³, Kai Cao^{1,2}, Gweltaz Mahéo³,**
5 **Yue Chen¹, Pan Zhang¹, Tianyi Shen¹, Guiling Wu¹, Paul Sotiriou⁴, Bo Wu¹**

6
7 1 Center for Global Tectonics, School of Earth Sciences, China University of Geosciences,
8 Wuhan, China.

9 2 State Key Laboratory of Geological Processes and Mineral Resources, China University of
10 Geosciences, Wuhan, China.

11 3 Laboratoire de Géologie de Lyon: Terre, Planètes et Environnement, Université Claude
12 Bernard, Villeurbanne, France.

13 4 School of the Environment, University of Windsor, Windsor, ON N9B 3P4, Canada.

14
15 **Corresponding author: Guocan Wang (wgcg@cgug.edu.cn)**

16
17 **Abstract**

18 Understanding the role of southeastern Tibet thrust faults in the development of the plateau
19 topography is key to our assessment of the geodynamic processes shaping the continental
20 topography. Detailed structure analysis along the ~400 km long Jinhe-Qinghe thrust belt
21 (JQTB) indicates post late Eocene thrust motion with a minor left-lateral component, inducing
22 ~0.6 to 3.6 km of apparent vertical offset across the fault. The exhumation history of the
23 Baishagou granite, based on the thermal modeling (QTQT) of new apatite (U-Th)/He and
24 fission-track ages, suggests an accelerated exhumation rate (~0.42 km/Myr) between 20 and 15
25 Ma, corresponding to ~1.7-2.4 km of exhumation. We interpret that fast exhumation as due to
26 the activation of the Nibi thrust, a northern branch of the JQTB resulting in the creation of
27 significant relief across the JQTB in the Early Miocene. When compared with previous studies
28 it appears that Cenozoic exhumation and relief creation in southeastern Tibet cannot be
29 explained by a single mechanism. Rather, at least three stages of relief creation should be
30 invoked. The first phase is an Eocene NE-SW compression partly coeval with Eocene
31 sedimentation. During the Late Oligocene to Early Miocene, coevally with Indochina extrusion,
32 the second thrusting phase occurred along the Yulong and Longmenshan thrust belts, and then
33 migrated to the JQTB at 20-15 Ma. A third phase involved the activation of the Xianshuihe

34 fault and the re-activation of the Longmenshan thrust belt and the Muli thrust. Uplift in the
35 hanging wall of thrust belts appears to explain most of the present-day relief in the southeastern
36 Tibetan Plateau.

37

38 **Key words:**

39 Southeast Tibet, low-temperature thermochronology, Jinhe-Qinghe thrust belt, Oligocene-
40 Miocene thrusting

41

42 **1 Introduction**

43 The Tibetan Plateau, the largest orogenic plateau on earth, results from complex crustal
44 deformation processes in the context of ongoing collision and indentation of the Indian and
45 Asian continents that commenced at least ca. 60-50 Ma ago (Molnar & Tapponnier et al., 1975;
46 Tapponnier et al., 2001; Hu et al., 2016). Many geodynamic models have been proposed to
47 explain the growth and expansion of the southeastern Tibet plateau. For example, the block
48 lateral extrusion model proposed rigid block escape along major boundary strike-slip faults,
49 and as a consequence, crustal shortening and thickening widely distributed on the margins of
50 the plateau (Tapponnier et al., 2001). Another model proposes that the crust thickened in the
51 interior of Tibet propagates toward the southeastern margin in the Middle Miocene through a
52 lower crustal flow generating the present-day continuous and gentle topography (Royden et al.,
53 1997; Clark et al., 2005). Southeastern Tibet is a key area to quantify the on-going process of
54 plateau migration and topography evolution because of the presence of upper crustal shortening
55 structures as well as elevated low-relief topography deeply dissected by large rivers as a result
56 of regional uplift and subsequent incision (Burchfiel et al., 1995; Tian et al., 2012; Clark et al.,
57 2005a; Liu-Zeng et al., 2008; Yang et al., 2016).

58 The recent GPS velocity field (Zhang et al., 2004) confirmed that the plateau material migrates
59 from the interior of Tibetan Plateau to the eastern and southeastern margin. Several studies
60 targeted at the boundary strike-slip faults between different blocks (e.g., Leloup et al., 1995,
61 2001; Replumaz et al., 2001; Xu and Kamp, 2000; Zhang et al., 2017; Wang et al., 2017). Many
62 other studies have been published on the Longmenshan (LMS) thrust belt. Only a few scattered
63 thermochronology data have been reported from the Yalong margin in the southwest
64 prolongation of the LMS (Figure 1), where thrust faults have been reported (Wang et al., 2012b;
65 Wu et al., 2019). Most studies suggest that these thrust faults are minor and that the main
66 Miocene thickening process is channel flow (e.g., Clark et al., 2005). Structural evidence of the
67 thrust faults is still lacking, and would play a vital role in thermochronology data interpretation.
68 Understanding the geometry and kinematics of these large-scale thrust faults, as well as thrust-
69 induced exhumation pattern, is crucial for deciphering the mechanism of extrusion and the
70 geomorphic evolution of the Tibetan Plateau.

71 In this paper, we re-assess the Jinhe-Qinghe thrust belt along the Yalong margin through the
72 utilization of detailed field structure analysis. New apatite fission track (AFT) and apatite (U-
73 Th)/He (AHe) ages collected along an elevation profile in the Jurassic Baishagou granite
74 located at the hanging wall of the Nibi thrust, a northern branch of the Jinhe-Qinghe thrust belt,
75 allows reconstruction of its cooling and exhumation history. That history provides a time

76 constraint on the activation of the Jinhe-Qinghe thrust belt. The Oligocene-Miocene structural
77 and relief evolution of southeastern Tibet will be discussed in light of these new data.

78 **2 Geological setting**

79 The Cenozoic tectonics of southeastern Tibet is marked by several large-scale strike-slip faults
80 including the Xianshuihe, Ailao Shan-Red River and Litang faults (Figure 1) (Allen et al., 1991;
81 Leloup et al., 1995; Zhang et al., 2015). North of the left-lateral Xianshuihe fault, a protracted
82 history of mountain building from the Upper Triassic to the present day, has been documented
83 in the NE-SW trending LMS thrust belt (Burchfiel et al., 1995; Roger et al., 2004; Wang et al.,
84 2012a; Tian et al., 2013). This thrust belt is located at the sharp topographic transition from the
85 Tibetan Plateau to the Sichuan Basin. South of the Xianshuihe fault the topographic transition
86 is less sharp but remains steep with the average elevation dropping from ~4200 m to ~1800 m
87 over a distance of 200-250 km (Liu-Zeng et al., 2008). Few detailed studies have focused on
88 the thrust faults in this area, however, NE-SW-trending faults (e.g., Jiulong, Muli, Yulong,
89 Jinhe-Qinghe faults) with apparent reverse motion appear on large-scale geological maps
90 (Figure 1) (Burchfiel et al., 1995; Wang et al., 2012a; Perrineau, 2010; Cao et al., 2019). The
91 Muli and Jinhe-Qinghe faults have been designated as the Yalong thrust belt and interpreted as
92 the southward continuation of the LMS thrust belt (Figure 1) (e.g., Burchfiel et al., 1995; Clark
93 et al., 2005; Wang et al., 2012b; Cao et al., 2019). The faults merge together before branching
94 on the left-lateral Xianshuihe fault, with a ca. 60 km offset. The absence of any flexural basin
95 and the relative smoothness of the relief drop with respect to that of the LMS led to the
96 hypothesis that the present-day topography mostly resulted from passive uplift above a lower
97 crustal channel flow that originated below central Tibet and veers around southern Sichuan,
98 rather than from thickening along the Yalong thrust belt (Clark et al., 2005). This uplift would
99 have warped up a low-relief erosion surface originally formed at low elevation, and induced
100 entrenchment of the major rivers. Low-temperature thermochronology suggests that this
101 entrenchment started at ~13-9 Ma, giving a proxy for the timing of surface uplift (Clark et al.,
102 2005; Ouimet et al., 2010). However, other studies document that other rivers in southeastern
103 Tibet underwent entrenchment from the Oligocene to early Miocene (30-20 Ma) (Shen et al.,
104 2016b; Tian et al., 2014). Detailed topographic studies indicate that the mean elevation drops
105 abruptly across the Muli thrust and JQTB (Liu-zeng et al., 2008; Wu et al., 2019). Based on
106 field observations and geological cross-sections, Perrineau (2010) estimated that ~12.5 km and
107 ≥ 22.5 km of horizontal shortening occurred across the JQTB and Muli fault, respectively, with
108 ~3.5 km of hanging wall uplift in both cases. Both the Yangtze and Yalong rivers exhibit large

109 bends when crossing the Yulong and Muli thrusts, respectively (Figure 1). Near the Yalong
110 bend, Wang et al. (2012b) interpret the Jinhe-Qinghe fault as a thrust fault with a left-lateral
111 component branching on the Xianshuihe fault. Moreover, Wang et al. (2012b) deduced from
112 the age versus elevation relationship of ten apatite fission track ages (AFT) that an increase in
113 the apparent cooling rate beginning at ~17 Ma was indicative of the onset of the fault. However,
114 the AFT samples appear to have been collected on the Jinhe-Qinghe fault footwall rather than
115 the hanging wall over a large horizontal distance of about 80 km (Figure 2), rendering this
116 constraint on the timing of fault onset unconvincing.

117 **3 Structural observations along the Jinhe-Qinghe Thrust Belt**

118 As described above, the Jinhe-Qinghe fault begins to branch progressively away from the Muli
119 fault from 28°40'N southwards (Figure 1, Figure 2). The Jinhe-Qinghe fault is split into several
120 branches (see below), accordingly, we would like to redefine it as the Jinhe-Qinghe thrust belt
121 (JQTB), rather than the Jinhe-Qinghe fault (Wang, et al., 2012b). The main fault stretches from
122 north of Mianning city to the Yongsheng area, east of the Chenghai thrust fault (Figure 1, Figure
123 2). Detailed structural analysis from six different sites along the JQTB is presented below.

124 3.1 Xilaping cross-section

125 This area is located near the western end of the main Jinhe-Qinghe fault, about 20 km to the
126 east of the Cheng Hai thrust. At site CD608 (Figure 2), a fault damage zone with unconsolidated
127 fault breccias and cataclastics, separates Sinian dolomite from Devonian siltstone (Figure 3a)
128 (Geol. map G47-11). The fault strikes NE-SW and dips 60-70° NW, to the northwest with an
129 apparent reverse motion (Figure 2a). The Sinian dolomite is affected by several faults (Figure
130 3b), with the main fault plane showing nearly downdip slickensides with crystallization steps
131 suggesting a thrust motion with a minor left strike-slip component (Figure 2a, 3d and 3h). In
132 the damage zone, ill-deformed dolomite lenses are surrounded by schistose levels. The lenses'
133 sigmoidal shapes are compatible with reverse motion in the fault zone (Figure 3b, 3f and 3g).

134 3.2 Tanjiawan cross-section

135 According to the published geological maps in the Tanjiawan area, the JQTB separates gray
136 Devonian limestone (D₂-D₃) from the siliciclastic rocks of the Eocene Hongyazi Fm. (Eh)
137 (Figure 2) (Geol. map G47-12; Wang et al., 2012b). Further northeast and to the south of the
138 Yanyuan, the Hongyazi Fm. is thought to be Late Eocene in age, according to mammal, plant
139 and Ostracoda fossils (Si et al., 2000). This observation is important as it implies that the JQTB
140 fault is younger than Late Eocene in age. The Hongyazi Fm. is composed of conglomerates

141 with limestone clasts at the bottom (Figure 4c) and purple/red fine-grained sandstone and
142 siltstone in the upper part (Geol. map G47-12). Stratifications in the Hongyazi Fm. dips to the
143 NW (Figure 4b) and unconformably overlap a Late Jurassic coal-bearing formation (Figure 4d).
144 The precise geometry of the JQTB is obscured because of heavy vegetation (Figure 4a-b),
145 however, it is likely a NE-SW fault that dips steeply to the NW. A cross-section indicates an
146 apparent vertical offset of the top of the Devonian of at least ~0.6 km and probably of ~2.1 km.
147 (Figure 4d).

148 North of the Tianjiawan basin, the geological maps show an NW-SE fault placing Sinian
149 dolomite and Paleozoic sediments on top of the Eocene rocks of the Ninglang basin (Figure 2)
150 (Geol. map G47-11; Gao et al., 2017). The fault is called the Lizihe-Ninglang fault (LNF)
151 (Wang et al., 2012b), and the Eocene sediments belong to the Ninglang Fm (En), which is quite
152 similar to the Hongyazi Fm. Wang et al. (2012b) inferred the sediments to be Oligocene to
153 Miocene in age. However, they are intruded by a series of granitic bodies (Figure 2, 4f) (Geol.
154 map G47-11), one of which has been dated at 33.1 ± 0.2 Ma (Early Oligocene) by zircon U-Pb
155 geochronology (Figure 4f, 4g; Table S1). This age confirms that the Ninglang Fm. is no younger
156 than Early Oligocene, and may have a similar age to the Hongyazi Fm., implying that the LNF
157 initiated after the Late Eocene-Early Oligocene. To the south, the LNF appears to be cut by a
158 branch of the JQTB (Figure 2) suggesting LNF could be older rather than a branch of JQTB.

159 3.3 Qinghe-Dalaluo cross-section

160 The middle segment of the JQTB is exposed on the road from Panzhihua to Yanyuan (section
161 C-C', Figure 2). In this area, the thrust belt veers from NNE-SSW to E-W and comprises two
162 branches with the southern one being the primary fault. According to the geological map, the
163 southern fault branch is itself composed of two splays, the lower, southern one trending N90°
164 and bringing Sinian rocks on top of Permian-Triassic rocks (Figure 5d). The apparent vertical
165 offset of the upper Devonian strata is estimated to be at least 700 m but more probably on the
166 order of ca. 3.6 km (Figure 5c). Our observations at site CD 461 show a large fault plane striking
167 N80° and dipping ~50° NNW that bears slickensides trending N298° (red planes in Figure 2b).
168 According to the geological map, the northern branch of the JQTB strikes N60° and brings
169 Devonian sediments on top of folded Carboniferous limestone with an apparant vertical offset
170 of the upper Devonian strata of ~1 km (Figure 5c and 5d). At site CD462, the bedrock is highly
171 fractured, and a series of subparallel secondary reverse faults form an imbrication zone with
172 roof and floor thrusts bounding a dolomite fragment and forming a duplex structure (Figure
173 5a). This geometry suggests a top to the east thrust motion (black planes in Figure 2b). A large

174 fault plane strikes $N5^{\circ} 35^{\circ}$ and bears slickensides trending $N338^{\circ}$ with steps suggesting left-
175 lateral (with minor thrust) motion (Figure 5b).

176 3.4 Jinhe cross-section

177 East of $100^{\circ}30'E$ the strike of the JQTB veers from NE-SW to N-S (Figure 2) (Figure 6g). The
178 JQTB can be continuously traced for more than 100 km from site CD461 of the Qinghe-Dalaluo
179 section until site 128, near the Jinhe town, where the fault strikes $N60^{\circ} 65^{\circ}N$ and places Sinian
180 rocks (gabbros and Sinian limestones) over Upper Permian basalts (Figure 6f, 6d). The fault
181 zone is complex with several parallel fault traces. Most faults dip steeply to the W, but locally
182 Devonian limestone is thrust over Triassic-Jurassic siltstone along a flatter surface (Figure 6f,
183 g). To the west, at site CD599, a fault strikes $N30^{\circ} 45^{\circ}W$ with the hanging wall comprising
184 Sinian and Paleozoic rocks, while drag folds are found adjacent to the fault zone implying a
185 thrusting movement (Figure 6a-c). From a cross-section (Figure 6f), the apparent vertical
186 component of motion on the JQTB can be estimated between 1.4 and 2.8 km according to the
187 offset of the base of the Triassic (Figure 6f).

188 East of the JQTB, Late Triassic siltstone with interbedded coal beds and Jurassic siltstone are
189 strongly folded by a series of anticlines and synclines with axes subparallel to steeply-dipping
190 N-S reverse faults, the most prominent one being the Hanjiawanzi fault that brings Triassic
191 rocks on top of Jurassic rocks (Figure 6f). Further east, Mesozoic sediments are separated from
192 the Aqi batholith by a west-dipping fault with an apparent normal throw that we term the Aqi
193 fault (Figure 6f) (Figure 2). Both the Hanjiawanzi and Aqi faults extend further to the south
194 (Figure 2).

195 3.5 Mianning–Yalong cross-section

196 North of the Jinhe cross-section the JQTB can be followed to the NNW to the Lizhuang area,
197 bringing Sinian rocks (Zbd) above Mesozoic sediments (Figure 2) (Geol. map G47-06). Near
198 Lizhuang, the JQTB and the Yalong fault branch together before turning to the NNE and
199 becoming progressively more linear closer to the Muli thrust (Figure.2). The kinematics of the
200 Yalong fault is thrust with a sinistral component which has been interpreted as a branch of the
201 JQTB (Wang et al., 2012b).

202 Sites CD733 and CD734 show evidences for \sim N-S-trending faulting. At site CD733, fault
203 gouge in the granite exhibits fault planes striking $N355^{\circ} 22^{\circ}N$ with slickensides striking $N265^{\circ}$,
204 indicative of dominating thrusting motion (Figure 2d, 7a-b). At site CD734, there is a tectonic
205 boundary between the yellow sandy slate and the black carbonaceous slate (Figure 7c). The
206 contact plane show undulations and strikes \sim $N30^{\circ}$ and dips $25\text{-}35^{\circ}W$ (Figure 2d). S-C fabrics

207 and asymmetric lens near the contact surface suggest left-lateral thrust motion (Figure 7d).
208 These two observation sites occur along the Nibi fault mapped ~8 km east of the Yalong fault
209 (figure 2) (Geol. map H47-36). To the south, the Nibi fault possibly extends to the Lizhuang
210 area (Wang et al., 2012b), as a branch of the JQTB. It is unlikely that the Nibi fault connects
211 with the Aqi fault, which is a normal fault in the south parallel to the J QTB (Geol. map G47-
212 06), while to the north its trace is obscured by Quaternary sediments.

213 At site CD760, west of the left-lateral Anninghe fault, a fault striking N50° separates Sinian
214 granites and Permian basalts (Figure 2) (Geol. map H48-31). Although the contact relationship
215 is unclear due to heavy vegetation, the granites and the Permian metamorphic basalts are
216 deformed and cataclastic near the contact (Figure 8b). Fault planes found in the basalt are nearly
217 vertical, strike ~N20° and show two groups of slickensides: one trending N15° and the other
218 one trending N210°. The former one shows left-lateral with minor thrust motion, while the latter
219 one shows left-lateral motion with a minor normal component (Figure 2e). In the field, the latter
220 crosscuts the former.

221 **4 Thermochronological constraints of the JQTB**

222 4.1 Sampling strategy and methods

223 Low-temperature thermochronology (e.g., fission track and (U-Th)/He) is widely used in
224 mountain building and landscape evolution to reconstruct the upper crustal cooling/exhumation
225 history (e.g., Shen et al., 2016a; Schildgen & Van der Beek., 2019). Complex structures and
226 strong topography affect isotherms in the upper crust which may significantly influence fission
227 track ages (Braun, 2002). To constrain the exhumation rate, it is thus better to sample along
228 vertical transects. We sampled an altitudinal transect (Baishagou transect) in the hanging wall
229 of the Yalong thrust over a relief of ~1000 m and culminating at 2443 m (Figure 2, 7e). The
230 horizontal distance of the Baishagou transect is ~ 1.3 km to reduce the topography effect as
231 much as possible. The nine samples were collected in an undeformed granite, the Jurassic
232 Baishagou granite (Figure 2) (Wang et al., 2014). They yielded nine AFT ages (Table 1) and
233 four AHe ages (Table 2). Neither deformation nor faults were detected in-between the samples.
234 Apatite fission track samples were dated by the LA-ICP-MS method (Gleadow et al., 2015).
235 Apatite grains were set in a regular array in epoxy resin and polished to expose a flat surface
236 for etching. Following this, the AFT grains were etched in 5 N HNO₃ at 21°C for 20 s to reveal
237 the spontaneous tracks. Sample preparation and spontaneous fission-track counting were
238 performed at the State Key Laboratory of Geological Processes and Mineral Resources, China
239 University of Geosciences, Wuhan, using the Autoscan system. In order to reduce the error due

240 to the low spontaneous track density, we tried to choose the largest grains and count the track
241 density in the area as wide as possible. The U content was measured by an Agilent 7700e LA-
242 ICP-MS at the State Key Laboratory of Geological Processes and Mineral Resources. The
243 parameters for laser ablation was set as 32- μm spot size, 4.5 J/cm² and 6 HZ repetition rate.
244 NIST 612 glass and ⁴³Ca of apatite were used as an internal standard to correct the U
245 concentrations of apatite aliquots.

246 AHe analyses were conducted at the University of Arizona, USA. Four grains without visible
247 inclusions and fracture per sample have been carefully selected. The radius and mass of each
248 grain was measured before dating. The grains were loaded into Nb tubes and heated with a laser
249 before cryogenic purification. Helium contents were measured using quadrupole mass
250 spectrometry. Subsequently, aliquots were dissolved in dilute HNO₃ and the U, Th, and Sm
251 contents have been obtained through ICP-MS (Ehlers & Farley, 2003). Measured ages have
252 been corrected by applying the α -ejection correction (Farley, 2002). Durango apatite grains
253 (31.4 ± 0.5 Ma) were analyzed together with our unknown age aliquots to check the reliability
254 and stability of the measurement.

255 4.2. Pseudo-elevation and age profile

256 The AFT ages from the Baishagou transect range between 26.9 Ma and 16.7 Ma and show a
257 strong relationship with altitude with all samples below 2198 m being younger than ~ 18.5 Ma
258 (Figure 9a). All ages were calculated from high-quality grains that have a homogeneous track
259 distribution, lack inclusions, and involved counting as large an area as possible. The χ^2 test of
260 all samples is $>5\%$ with low age dispersion, indicating a single age population. The three AHe
261 ages gave similar ages at ~ 15 Ma. To ensure a better interpretation of the exhumation history,
262 an AFT age vs elevation (Figure 9a) and a composite AFT and AHe age vs pseudo-elevation
263 (Figure 9b) diagram were plotted. For the pseudo-elevation diagram, the AHe ages were plotted
264 against true elevation, while the AFT ages elevations were increased by a constant value
265 calculated from the closure temperature difference between the AFT and AHe systems (Reiners
266 and Brandon, 2006). Assuming a geothermal gradient of 30 °C/km, a closure temperature of 65
267 °C and 110 °C for AHe and AFT thermochronometric systems respectively (Farley, 2002;
268 Wagner and van den Haute, 1992) suggests an increase in elevation of 1500 m.

269 Sample CD753 yielded three AHe grain ages (Table 2), however, two of them are older than
270 the corresponding AFT age (16.9 ± 1.4 Ma), probably caused by U/Th zoning (Farley et al.,
271 2011), radiation damage (Shuster et al., 2006) or inclusions (Vermeesch et al., 2007), and have

272 been discarded. Furthermore, we prefer to not use the third single crystal age whose
273 reproducibility cannot be tested and thus not consider sample CD753 AHe age.

274 The obtained plot can be interpreted in two different ways (Fig 9b).

275 (1) A single event model corresponding to one constant Oligocene-Miocene exhumation. The
276 mean exhumation rate calculated by the single least-squares regression slope is ~ 0.15 km/Myr
277 with a relatively low correlation coefficient ($R^2=0.69$), and two AFT and two AHe samples
278 outside of the 95% confidence interval (grey array on Figure 9b).

279 (2) A two episodes exhumation history, with a break in slope at 2200 m and ~ 19 Ma (blue
280 arrays, Figure 9b). The linear regression of the upper part of the profile corresponds to a very
281 slow exhumation rate of ~ 0.03 km/Myr ($R^2=0.99$), while the lower part shows a relatively rapid
282 exhumation of ~ 0.31 km/Myr between ~ 19 and 14 Ma ($R^2=0.90$) that would correspond to at
283 least 1700 m of exhumation.

284 Given the difference in age between the AFT and AHe for a given sample, this can yield
285 estimates of the cooling rate. Assuming that the closure temperature of AFT and AHe system
286 is 65°C and 110°C respectively (Farley, 2002; Wagner and van den Haute, 1992), the rates
287 would be $\sim 4^\circ\text{C/Ma}$ between ~ 27 and 15 Ma for CD746, $\sim 7^\circ\text{C/Ma}$ between ~ 22 and 15 Ma for
288 CD747, and $\sim 11^\circ\text{C/Ma}$ between ~ 19 and 14 Ma for CD749. This suggests that the cooling rate
289 significantly increased after 19 Ma. This strongly suggests that the increase in the cooling rate
290 is correlated with the increase in the exhumation rate outlined in the two stages model (Figure
291 9b) and thus that it reveals an increase in the exhumation rate at ~ 19 Ma. Furthermore, the two
292 highest samples (CD746 and CD747, Table 1) show shorter track lengths than the other samples
293 (Table 1) indicating that they stayed in the AFT PAZ during the slow cooling phase until ~ 22
294 Ma prior to cool rapidly together with the other samples.

295 4.3. Thermal Modeling

296 To better constrain the cooling and exhumation history of the Baishagou granite, we performed
297 QTQt modeling (Gallagher, 2012) based on the nine AFT ages and three AHe ages. In this
298 model, prior constraints are as follows: (a) the present-day surface temperature is $10 \pm 10^\circ\text{C}$;
299 (b) the default geothermal gradient is $\sim 30 \pm 30^\circ\text{C/km}$. (c) The temperature offset was permitted
300 to vary over time because of the unstable paleo-geothermal gradient. (d) We did not dispose of
301 any precise and reliable constraints on the temperature-time history of the Baishagou granite
302 and the QTQt models were performed without any external constraint, to avoid
303 overinterpretation of the modeling result (Vermeesch & Tian, 2014). (e) 100,000 burn-in and
304 post-burn-in iterations were performed for the modeling to get a stable result. The modeling

305 results are shown in Figure 10, including the maximum likelihood model and the expected
306 model derived from the QTQt inverse modeling.

307 The maximum likelihood model corresponds to the model with the lowest misfit with the data
308 (Gallagher, 2012). It reproduces well the AFT and AHe ages and the track length data (Figure
309 10a, b). This model presents a three-stage cooling history. First ~20 Ma of slow cooling from
310 ~140 to 130 °C at a rate of ~0.5 °C/Myr, second rapid cooling between 20 and 15 Ma at a rate
311 of 10 °C /Myr, and third slow cooling from ~60-40°C at a rate of ~2 °C/Myr (Figure 10a). The
312 timing of initiation of the fast cooling phase at ~20 Ma is similar to the timing of the break-in
313 slope in the pseudo-elevation age profile (Figure 9b). Subsequently, the rocks underwent a
314 faster cooling that we interpreted to have resulted from the rapid exhumation of the rocks.
315 Taking the geothermal gradient calculated from the QTQt model (30 °C/km for the first episode
316 and 26 °C/km for the others), the exhumation rate between 20 and 15 Ma is 0.415 ± 0.075
317 km/Myr corresponding to ~1.7-2.4 km of total exhumation. After ~15 Ma, a period of slow
318 cooling corresponds to less than ~1 km of exhumation.

319 The expected model is a weighted mean model that yields a range of possible cooling histories
320 at a 95% range for each parameter and is expected to show smoother cooling histories than the
321 maximum likelihood model (Gallagher, 2012). As a matter of fact, the results show a more
322 progressive transition from slow (~1-2 °C/Myr) to relatively fast cooling (~7-8 °C/Myr) to at
323 about 24-20 Ma, followed by a stage of moderate cooling (~2-3 °C/Myr) after ~15-11 Ma
324 (Figure 10c). The fit between predicted and observed ages in this model is not as good as the
325 maximum likelihood model, even though the results are within the error bars (Figure 10d).

326 To conclude, both models imply a relatively fast cooling period (10 to 7 °C/Myr) between 24-
327 20 and 15-11 Ma, which we interpret as the result of rapid exhumation.

328 **5 Discussion**

329 5.1 Exhumation mechanism(s) of the Baishagou granite

330 Few published thermochronology studies have focused on the exhumation of the Yalong region
331 of the JQTB (Figure 1). Wang et al. (2012b) reported a fast exhumation at ~17 Ma derived from
332 AFT samples scattered along a ~80 km horizontal distance in the footwall of the Yalong fault
333 (Figure 2). Upstream along the Yalong river, Clark et al. (2005) reported ~13-9 Ma rapid river
334 incision from samples collected from the upper wall of the Muli thrust fault. Our data imply
335 that the fast cooling of the Baishagou granite occurred between 24-20 and 15-11 Ma. It is more
336 likely that this cooling occurred between 20 and 15 Ma at a rate of 10°C/Ma and corresponds
337 to ~1.7-2.4 km of exhumation at a rate of ~0.4 km/Myr. The granite lies in the deep Yalong

338 river gorges in the footwall of the Muli thrust and the hanging wall of the Yalong and Nibi
339 faults (Figure 2). Two main processes can be proposed for exhumation: fluvial erosion or uplift
340 in the hanging wall of a thrust fault. However, a more regional uplift mechanism cannot be
341 ruled out. For example, some workers have linked the deep erosion of the Yalong river to lower
342 crustal flow at depth that would have propagated from the Tibetan Plateau towards the southeast
343 during the Late Miocene (~13 Ma) (Clark & Royden, 2000; Clark et al., 2005; Ouimet et al.,
344 2010). As discussed above the timing of exhumation of the Baishagou granite is constrained to
345 start ~20 Ma, which is significantly older than the age proposed for the onset of exhumation
346 linked with lower crustal channel flow in that area (~13 Ma, Clark & Royden, 2000; Clark et
347 al., 2005). This will be discussed in more detail below.

348 The Anninghe fault is an active left-lateral strike-slip fault that is the southern extension of the
349 Xianshuihe fault system and is located along the Anninghe River 32 km east of the Baishagou
350 granite (Figure. 2). This fault could have played a role in the exhumation of the Yalong area.
351 However, it is a strike-slip fault with a very small vertical component that could probably not
352 have induced the ~2 km exhumation recorded in the Baishagou region. For example, the
353 slickensides observed at site CD760 probably belong to a branch of the Anninghe fault and
354 show very little vertical component (Figure 2). Furthermore, the fault is the prolongation of the
355 Xianshuihe fault, which is considered to be younger than 9 Ma (Zhang et al, 2017), or even
356 possibly ~5 Ma (Wang et al., 2009) at this location.

357 Alternatively, several faults straddle the Mianning-Yalong zone (Figure 2, Figure 7e) and could
358 have induced the exhumation of the Baishagou granite. The Muli fault is an NW dipping thrust
359 outcropping 12 km to the NW and would thus induce subsidence, not uplift, of the Baishagou
360 granite. Alternatively, the granite lies in the hanging wall of the Yalong and Nibi thrusts (Figure
361 2, Figure 7e). Wang et al. (2012b) provided the AFT ages of ten samples from four locations in
362 between the Yalong and Nibi faults (Figure 2). When plotted together with our data, their ages
363 define roughly the same age versus altitude relationship implying a strong common exhumation
364 between ~20 and 15 Ma (Figure 9a). Because all these samples are in the hanging wall of the
365 Nibi fault, it suggests that this fault is responsible for this exhumation. The upper part of the
366 plot, however, possibly shows a ≤ 7 Ma offset between the two data sets (Figure 9a). Such offset
367 could result from a faster exhumation of the samples west of the Yalong fault until ~20 Ma,
368 which would be compatible with a small reverse motion on the fault at that time. After 20 Ma,
369 both data sets show fast exhumation that we have constrained to be at ~0.4 km/Ma until 15 Ma
370 from the QTQt modeling of our data. Data from Wang (2012b) suggest that fast exhumation
371 lasted until ~15 Ma and was followed by a slower exhumation phase (Figure 9a), suggesting

372 that the Nibi fault ceased at that time. A 1300 m elevation difference is observed from the
373 Anninghe valley bottom to the ridge in the hanging wall of the Nibi fault. We suggest that most
374 of this difference results from the ~1.7-2.4 km early Miocene fast exhumation in the hanging
375 wall of the Nibi fault.

376 5.2 Timing of the Jinhe-Qinghe Thrust Belt

377 As described above, the JQTB runs for more than 300 km from the Yalong-Mianning area to
378 the Xilapin area, bringing Sinian rocks on top of Mesozoic sediments (Figure 2). Our field
379 observations confirm that the JQTB is a thrust with ~0.6 to 3.6 km of apparent vertical offset.
380 Locally, the JQTB shows a large left-lateral component (Figure 2b – site CD462, d), but where
381 it trends E-W it shows a right-lateral component (Figure 2b – site CD461). The amount of
382 strike-slip displacement is difficult to estimate and is most probably small. In Tanjiawan,
383 Eocene sediments are found in the footwall of the JQTB implying that the fault is younger than
384 33.1 ± 0.2 Ma (Figure 4g).

385 In the Mianning-Yalong zone, the Nibi thrust was active since ~20 Ma. The prolongation of the
386 thrust to the south is not clear, but one possibility is that it is a branch of the JQTB (Figure 2).
387 The amount of exhumation between 20 and 15 Ma in the hanging wall of the Nibi fault
388 constrained from the thermochronology data is ~1.7-2.4 km, which is on the same order than
389 the ~0.6 to 3.6 km of apparent offset on the JQTB. This confirms that the Nibi fault is the
390 northern prolongation of the JQTB that has been active between ~20 and ~15 Ma.

391 5.3 Regional tectonic implications

392 5.3.1 Compatibility with the channel flow model

393 One of the processes that have been invoked for the uplift/exhumation of the southeastern Tibet
394 margin is a flow of partially molten lower crust pushed outward from the Tibetan Plateau by
395 body forces due to its exceptional thickness. The flow would be halted and pushed upward by
396 the stiff Sichuan craton to create the LMS range, while it would be continuous across the
397 Yunnan margin inducing a smoother relief. In that model, an uplift wave would progressively
398 propagate from west to east, inducing river incision and erosion ((Clark & Royden, 2000; Clark
399 et al., 2005). The Yalong river incision at 13-9 Ma derived from AFT and AHe data was taken
400 as a proxy for river incision and thus the propagation of channel flow across the Yalong margin
401 (Clark et al., 2005; Ouimet et al., 2010).

402 However, a growing number of studies document erosion/exhumation timings that are not in
403 accord with the channel flow hypothesis, i.e. a simple propagation from west to east through

404 time (Figure 1). For example, surface uplift in the Daocheng took place between ~22 and 15
405 Ma (Figure. 1) (Tian et al., 2014), whilst other fast exhumation of the hanging wall along the
406 Jiulong thrust fault took place at ~35-30 Ma and between 8 and 7 Ma (Zhang et al., 2016). Near
407 Xiangcheng, the fast exhumation and entrenching of the Shuoqu River (upper reach of the
408 Yangtze River) lasted from 18-15 to 12 Ma (Gourbet et al., 2019). Along the Jiulong River,
409 incision started at 13-9 Ma (Clark et al., 2005), whilst our study located further downstream of
410 the Yalong river and 15 km east, documents exhumation starting at ~20 Ma. Such timing is
411 incompatible with a channel flow model for the entrenching of the Yalong river.

412 5.3.2 Diachronous Cenozoic exhumation of southeastern Tibet

413 In the LMS region, two main episodes of rapid exhumation phases during the Cenozoic have
414 been documented. In the central LMS region, these two phases have been dated by low-
415 temperature thermochronology in the Pengguan range at 30-25 to 25-20 Ma (Wang et al., 2012a)
416 and ~11 Ma to the present day (Godard, 2009; Wang et al., 2012a). This has been interpreted
417 as two episodes of mountain building, the younger one is still active as shown by the Wenchuan
418 earthquake. In the southwest LMS, the exhumation of the Baoxing granite started prior to 17-
419 15 Ma, while the exhumation in the hanging wall of the Wulong fault started at 12-10 Ma (Cook
420 et al., 2013) (Figure 1).

421 The left-lateral Xianshuihe fault separates the southern LMS from the Yalong thrust (Figure.
422 1). The total offset has been estimated at ~60 km (e.g., Wang et al., 1998; Wang and Burchfiel,
423 2000; Yan and Lin, 2015). The timing of onset is disputed, however, Zhang et al. (2017)
424 proposed that it initiated at 12.6 ± 1 Ma in the NW (Wang et al., 2009) and propagated between
425 the LMS and Yalong thrust at ~9 Ma.

426 Tapponnier et al. (2001) suggested that the thrusts of the Yalong margin correspond to thrusts
427 branching on the Xianshuihe fault during the Eocene-Oligocene. Wang et al. (2012b) also
428 suggested that the JQTB was a thrust with a large left-lateral component branching of the
429 Xianshuihe fault active at ~17 Ma (Middle Miocene). Our results confirm the timing proposed
430 by Wang et al. (2012b), however, this hypothesis does not fit with the age of the Xianshuihe
431 fault which is significantly younger in that area (~9 Ma) (Zhang et al., 2017).

432 To the SW, the JQTB seems to cut the LNF (Figure 2). The LNF thrust is younger than Eocene
433 sediments older than 33.15 ± 0.21 Ma. The LNF trends NNW-SSE almost parallel to the
434 Chenghai and Yulong thrusts. The age of the Yulong thrust has been proposed to be between
435 28 and 20 Ma (Cao et al., 2019), coeval with E-W compression and left-lateral shear along the

436 Ailao Shan-Red River (ASRR) shear zone (Leloup et al., 1995, 2001, 2007). An age of 28 to
437 20 Ma for the LNF would be compatible with the age that we propose for the JQTB (20-15 Ma).
438 It thus appears that a single model cannot explain all the exhumation ages now available in
439 southeastern Tibet and that one should envisage several exhumation mechanisms taking place
440 during a multistage history.

441 5.3.3 Multistage history for the growth of relief in the southeastern Tibetan Plateau

442 The growing data set on the timing of exhumation, including the present study and paleo-
443 altimetry suggest that several mechanisms contributed to the formation of the present-day
444 topography in southeastern Tibet. Below we list several tectonic events that have contributed
445 to the topographic growth of eastern Tibet.

446 Mesozoic deformation has been widely documented in the eastern Tibet (e.g., Roger et al.,
447 2010), and Cretaceous deformation and metamorphism occurred in the south LMS (e.g.,
448 Airaghi et al, 2018) and Danba area (Wallis et al., 2003). These events have probably produced
449 significant relief. However, it is unclear how much of that relief was preserved prior to the Early
450 Eocene at the time of the India-Asia collision. The Jianchuan Eocene basin formed in the
451 footwall of the Ludian-Zhonghejiang thrust that was active between 50 and 39 Ma according
452 to low-temperature thermochronology (Figure 1, Figure 11) (Cao et al., 2020). Such
453 deformation implies NE-SW shortening (in present-day coordinates) (Figure 12a) and is
454 comparable to deformation and sedimentation of the HohXil and Yushu-Nangqian basins
455 further west in the Tibetan Plateau (Horton et al., 2002; Spurlin et al., 2005; Staisch et al., 2016).
456 Such deformation produced crustal shortening responsible for significant relief creation. Indeed,
457 some paleo-elevation studies indicate that parts of southeastern Tibet reached high elevation
458 before the Oligocene: Liming basin, 2650 ± 300 m at ≥ 40 Ma (Hoke et al., 2014), the Jianchuan
459 basin, 2.9 ± 0.6 km at ~ 36 Ma (Wu et al., 2018), the Gonjo basin, ≥ 2100 - 2500 m at ≥ 43 Ma
460 (Tang et al., 2017), the Markam basin, ~ 3 km at ~ 34 Ma (Su et al., 2018). However, studies
461 relying on $\delta^{18}\text{O}$ measurements probably overestimated the paleo-elevations (Botsyun et al.,
462 2019). For example, in the Jianchuan basin, the Eocene (~ 36 Ma) altitude could be re-evaluated
463 to 1200 ± 1200 m depending on the assumptions made for the Eocene conglomerates (Gourbet
464 et al., 2017; Wu et al., 2018). In any case, at least 1 to 2 km of altitude needs to have been
465 gained after the Eocene in western southeastern Tibet and probably much more in the rest of
466 the area.

467 During the Late Eocene-Early Oligocene (35-30 Ma) only one phase of exhumation is
468 documented in eastern Tibet, which is in the hanging wall of the Jiulong thrust (Figure 11,

469 Figure 12a) (Zhang et al., 2017). That time corresponds to a major phase of ultrapotassic
470 magmatism dated between 36.9 and 32.5 Ma. (Schärer et al., 1994; Liang et al., 2007; Chung
471 et al., 2008; Lu et al., 2012). The products of this magmatism are found in a zone with a diameter
472 of ~200 km that was later cut and offset ~600 km by the left-lateral ASRR (Leloup et al., 2001).
473 A phase of magmatism at ~33 Ma followed by rapid cooling until ~29 Ma in the Xuelong Shan
474 range has been interpreted as taking place after the onset of the shear zone (Leloup et al., 2001;
475 Leloup et al., 2007). Gourbet et al. (2017) proposed that doming of the upper crust under the
476 effect of rising magmas due to ultrapotassic magmatism (Figure 12a) would have been
477 sufficient to provoke a major drainage reorganization. Other studies have linked the
478 ultrapotassic magmatism to lithospheric delamination (Chung et al., 1998, 2005; Lu et al., 2012),
479 in which case it would have induced a large regional uplift. However, such a hypothesis would
480 require extension, rather than compression, at the time of magmatism.

481 In the Late Oligocene-Early Miocene (30-20 Ma) (Figure 12b), a major phase of exhumation
482 has been documented interpreted as resulting from a first phase of thrusting along the LMS
483 thrust belt (Figure 11) (Wang et al., 2012a), indicating ~NW-SE compression.
484 Contemporaneous exhumation (28-20 Ma) of the Jianchuan basin has been interpreted to be
485 linked to the Yulong thrust fault (Cao et al., 2019) suggesting ~WNW-ESE compression. The
486 Chenghai and LNF thrust most probably activated at the same time (Wang et al., 2012b; Cao et
487 al., 2019). This resulted in the creation or amplification of the relief in the hanging wall of the
488 faults (Figure 12b). As both the Yulong and LMS thrust belts were active at this time, it is
489 tempting to consider that the Muli fault located in between would have also been active. The
490 later activity of that fault is likely based on low-temperature thermochronology (see below),
491 however, the lack of higher temperature thermochronology data precludes any definitive
492 answer.

493 During 20-15 Ma, the Nibi thrust was active and thus most probably the Jinhe-Qinghe thrust
494 (Figure 12c), with 0.6 to 3.6 km of apparent vertical offset inducing 1.7 to 2.4 km exhumation
495 of the hanging wall. Relief creation in the hanging wall of the Jinhe-Qinghe thrust expanded
496 the high Tibetan relief to the southeast. Differential uplift is still visible in the ~1200 m
497 topographic step across the JQTB (Perrineau, 2010; Wu et al., 2019). No significant exhumation
498 has been documented in the central LMS, however, Cook et al. (2013) report a phase of
499 exhumation starting prior to 15 Ma in the Baoxing granite, which is located in the hanging wall
500 of the Erwangmiao fault in the southwestern LMS (Figure 12c). At 15 Ma, all parts of the
501 topographic transition from Tibet to areas of lower elevation had been uplifted and the relief
502 could have been comparable to the present-day relief. Correspondingly, the clastic sediments

503 denudated from southeastern Tibetan Plateau were transported to the South China Sea by large
504 river systems (e.g., Paleo-Red River) with peaks in the sediment flux at ~19 Ma and 17-15 Ma
505 (Clift et al., 2006, 2014), which fits our proposed 20-15 Ma accelerated exhumation very well.
506 The extrusion of Indochina along the ASRR ended at ~17 Ma (Leloup et al., 2001) marking a
507 major tectonic change in the area. One could expect that the Jiulong and Muli thrusts and JQTB
508 would have been activated in that order following the propagation of the Tibetan Plateau toward
509 the southeast, or an in-sequence thrusting from the plateau interior. This is based on the fast
510 exhumation documented at the thrust fault hanging walls of the Jiulong, Muli and Nibi (JQTB)
511 thrusts that show phases of rapid cooling at between ~35 and 30 Ma and between 8 and 7 Ma
512 (Zhang et al., 2016), between ~13 and 5 Ma (Clark et al., 2005) and between 20 and 15 Ma (this
513 study), respectively (Figure 1, Figure 12a-c). Higher temperature thermochronology system
514 (ZHe and ZFT) focusing on the Muli thrust will possibly provide more information about the
515 earlier exhumation phase of the Muli thrust and its mechanism.

516 After the end of Indochina extrusion, the left-lateral Xianhuihe fault initiated at ~13 Ma in the
517 northwest (Wang et al., 2009) and propagated to the southeast, reaching the Gongga Shan area
518 at ~9 Ma (Zhang et al., 2017), and further to the southeast probably at ~4 Ma (Figure 12d). The
519 dextral Red River fault initiated along the former ASRR possibly at ~12 Ma (Leloup et al.,
520 2001; Wang et al., 2016), or at ~5 Ma (Leloup et al., 1993), when several N-S normal faults re-
521 activated previous thrusts. Between 12 and 8 Ma, several NE-SW thrusts initiated: the Muli
522 fault in the Yalong margin (Pitard et al., submitted), the Wulong fault in the southern LMS
523 (Cook, 2013) and the Beichuan fault in the central LMS (Godard et al., 2009) (Figure 12d). In
524 the two first cases, this implies a late activation of internal faults.

525 **6. Conclusions**

526 Detailed field observations along the Jinhe-Qinghe thrust belt and low-temperature
527 thermochronology (AFT and AHe dating) from the hanging wall of the Nibi thrust, branch of
528 the JQTB yield new constraints on the amount and timing of thrusting in southeastern Tibet.
529 The structure analysis shows that the JQTB is a post-Eocene thrust with several branches, with
530 total apparent vertical offset on the order of ~0.6 to 3.6 km. The pseudo-elevation-age profile
531 and QTQt modeling of the Baishagou granite show that fast exhumation occurred between 20-
532 15 Ma in the hanging wall of the Nibi thrust at a rate of ~0.42 km/Myr corresponding to ~1.7-
533 2.4 km of total exhumation. Thrusting movement of JQTB was most probably responsible for
534 this rapid exhumation and created significant relief in SE Tibet during the Miocene.

535 When considering previous studies, it appears that Cenozoic exhumation and relief creation in
536 southeastern Tibet does not follow a simple pattern that could be explained by a single
537 mechanism. Building from relict reliefs from previous tectonic events (i.e., Triassic and
538 Cretaceous), at least three stages of Cenozoic shortening and relief creation have to be invoked.
539 The first stage was marked by Eocene NE-SW compression at least partly coeval with the
540 sedimentation of the Eocene sediments. The second stage during the Late Oligocene to Early
541 Miocene corresponds to an NW-SE to E-W compression yielding to thrusting in the LMS, and
542 the Yulong thrust belt. The activity of the JQTB is posterior to that event, corresponding to a
543 southeastern migration of the high plateau through time. A third stage corresponds to the
544 activation of left-lateral strike-slip faults such as the Xianshuihe fault and the re-activation of
545 thrusts such as the Beichuan and Wulong faults in the LMS and the Muli thrust. The precise
546 interaction between thrusting and fast river erosion driven by Miocene monsoon strengthening
547 as documented around 11-8 Myr ago (An et al., 2001; Zachos et al., 2001; Allen et al., 2012)
548 has not been deciphered yet, but Oligocene - Miocene thrusting appears to explain most of the
549 present-day relief in southeastern Tibet.

550 **Data Availability**

551 All the data documented are listed in the references or archived in Figshare repository
552 ([10.6084/m9.figshare.13148498](https://doi.org/10.6084/m9.figshare.13148498)).

553 **Acknowledgments**

554 We thank Kerry Gallagher for providing us the new version of modeling software and the
555 guidance of QTQt modeling. We are also grateful to Andrew Gleadow for the helpful
556 suggestions about the fission track dating based on LA-ICP-MS. This work is funded by the
557 National Science Foundation of China (41672195). We thank two anonymous reviewers that
558 provided constructive comments on an early version of the manuscript.

559 **REFERENCES**

- 560 Airaghi, L., de Sigoyer, J., Guillot, S., Robert, A., Warren, C. J., Deldicque, D., 2018. The
561 Mesozoic along-strike tectonometamorphic segmentation of Longmen Shan (eastern
562 Tibetan plateau). *Tectonics* 37, 4655–4678. <https://doi.org/10.1029/2018TC005005>.
- 563 Allen, C.R., Luo, Z.L., Qian, H., Wen, X.Z., Zhou, H.W., Huang, W.S., 1991. Field study of a
564 highly active fault zone: the Xianshuihe fault of southwestern China. *Geological Society
565 of America Bulletin* 103, 1178–1199. [https://doi.org/10.1130/0016-
566 7606\(1991\)103<1178:FSOAHA>2.3.CO;2](https://doi.org/10.1130/0016-7606(1991)103<1178:FSOAHA>2.3.CO;2).
- 567 Allen, M.B., & Armstrong, H.A., 2012. Reconciling the Intertropical Convergence Zone,
568 Himalayan/Tibetan tectonics, and the onset of the Asian monsoon system. *Journal of Asian
569 Earth Sciences* 44, 36–47. <https://doi.org/10.1016/j.jseaes.2011.04.018>.
- 570 An, Z.S., Kutzbach, J.E., Prell, W.L., Porter, S.C., 2001. Evolution of Asian monsoons and
571 phased uplift of the Himalaya-Tibetan plateau since late Miocene times. *Nature* 411, 62–
572 66. <https://doi.org/10.1038/35075035>.
- 573 Botsyun, S., Sepulchre, P., Donnadieu, Y., Risi, C., Licht, A., Rugenstein, J.K.C., 2019.
574 Revised paleoaltimetry data show low Tibetan Plateau elevation during the Eocene.
575 *Science* 363, 946. <https://doi.org/10.1126/science.aag1436>.
- 576 Braun J., 2002. Quantifying the effect of recent relief changes on age–elevation relationships.
577 *Earth and Planetary Science Letters* 200, 331–343. [https://doi.org/10.1016/S0012-
578 821X\(02\)00638-6](https://doi.org/10.1016/S0012-821X(02)00638-6).
- 579 Burchfiel, B. C., Chen, Z. L., Liu, Y. P., Royden, L. H., 1995. Tectonics of the Longmen Shan
580 and adjacent regions, central China. *International Geology Review* 37, 661–735.
581 <https://doi.org/10.1080/00206819509465424>.
- 582 Bureau of Geology and Mineral Resources of Sichuan Province (map G47-06, G47-12, G48-
583 01, H47-36, H48-31, scale 1:200,000), 1991. Regional geology of Sichuan Province,
584 Geological Publishing House, Beijing.
- 585 Bureau of Geology and Mineral Resources of Yunnan Province (map G47-11, scale 1:200,000),
586 1990. Regional Geology of Yunnan Province, Geological Publishing House, Beijing.
- 587 Cao, K., Wang, G.C., Leloup, P. H., Mahéo, G., Xu, Y.D., van der Beek, P. A., et al., 2019.
588 Oligocene-Early Miocene topographic relief generation of southeastern Tibet triggered by
589 thrusting. *Tectonics* 38 (1), 374–391. <https://doi.org/10.1029/2017TC004832>.
- 590 Cao, K., Leloup, P.H., Wang, G.C., Liu, W., Mahéo, G., Shen, T.Y., et al., 2020. Thrusting,
591 exhumation, and basin fill on the western margin of the South China block during the
592 India-Asia collision. *Geological Society of America Bulletin*
593 <https://doi.org/10.1130/B35349.1>.
- 594 Chung, S.-L., Lo, C.-H., Lee, T.-Y., Zhang, Y., Xie, Y., Li, X., et al., 1998. Diachronous uplift
595 of the Tibetan plateau starting 40 Myr ago. *Nature* 394 (6695), 769–773.
596 <https://doi.org/10.1038/29511>.
- 597 Chung, S.-L., Chu, M.-F., Zhang, Y., Xie, Y., Lo, C.-H., Lee, T.-Y., Wang, Y., 2005. Tibetan
598 tectonic evolution inferred from spatial and temporal variations in post-collisional

599 magmatism. *Earth-Science Reviews* 68 (3–4), 173–196.
600 <https://doi.org/10.1016/j.earscirev.2004.05.001>.

601 Clark, M.K., & Royden, L.H., 2000. Topographic ooze: building the eastern margin of
602 Tibet by lower crustal flow. *Geology* 28, 703–706. [https://doi.org/10.1130/0091-7613\(2000\)28<703:TOBTEM>2.0.CO;2](https://doi.org/10.1130/0091-7613(2000)28<703:TOBTEM>2.0.CO;2).

603
604 Clark, M.K., House, M.A., Royden, L.H., Whipple, K.X., Burchfiel, B.C., Zhang, X., Tang,
605 W., 2005. Late Cenozoic uplift of southeastern Tibet. *Geology* 33, 525–528.
606 <https://doi.org/10.1130/G21265.1>.

607 Clift, P.D., 2006. Controls on the erosion of Cenozoic Asia and the flux of clastic sediment
608 to the ocean. *Earth and Planetary Science Letters* 241, 571–580. <https://doi.org/10.1016/j.epsl.2005.11.028>.

609
610 Clift, P.D., Wan, S.M., Blusztajn, J., 2014. Reconstructing chemical weathering, physical
611 erosion and monsoon intensity since 25 Ma in the northern South China Sea: A review of
612 competing proxies. *Earth-Science Reviews* 130 2014 86–102. <https://doi.org/10.1016/j.earscirev.2014.01.002>.

613
614 Cook, K. Royden, L., L. H., Burchfiel, B. C., Lee, Y. H., Tan, X., 2013. Constraints on
615 Cenozoic tectonics in the southwestern Longmen Shan from low-temperature
616 thermochronology, *Lithosphere* 5(4), 393–406. <https://doi.org/10.1130/L263.1>.

617 Ehlers, T.A., 2005. Crustal thermal processes and the interpretation of thermochronometer
618 data. *Rev. Mineral. Geochem.* 58, 315–350. <https://doi.org/10.2138/rmg.2005.58.12>.

619 Farley K.A., 2002. (U–Th)/He dating: Techniques, calibrations, and applications. *Rev Mineral*
620 *Geochem.* 47(1):819–844. <https://doi.org/10.2138/rmg.2002.47.18>.

621 Farley, K. A., Shuster, D. L. Ketcham, R. A., 2011. U and Th zonation in apatite observed by
622 laser ablation ICPMS, and implications for the (U–Th)/He system. *Geochimica et*
623 *Cosmochimica Acta* 75, 4514–4530. <https://doi.org/10.1016/j.gca.2011.05.020>.

624 Gallagher, K., 2012. Transdimensional inverse thermal history modeling for quantitative
625 thermochronology. *Journal of Geophysical Research* 117, B02408. <https://doi.org/10.1029/2011JB008825>.

626
627 Gao, L., Yang, Z.Y., Tong, Y.B., Wang, H., An, C.Z., Zhang, H.F., 2017. Cenozoic clockwise
628 rotation of the Chuan Dian Fragment, southeastern edge of the Tibetan Plateau: Evidence
629 from a new paleomagnetic study. *Journal of Geodynamics* 112 (2017), 46–57.
630 <https://doi.org/10.1016/j.jog.2017.10.001>.

631 Ge Y.K., Liu-Zeng, J., Zhang J.Y., Wang W., Tian Y.T., Fox M., et al., 2020. Spatio-temporal
632 variation in rock exhumation linked to large-scale shear zones in the southeastern Tibetan
633 Plateau. *Science China Earth Sciences* 63, 512–532. <https://doi.org/10.1007/s11430-019-9567-y>.

634
635 Godard, V., Pik, R., Lave, J., Cattin, R., Tibari, B., de Sigoyer, J., Pubellier, M., Zhu, J., 2009,
636 Late Cenozoic evolution of the central Longmen Shan, eastern Tibet: Insight from (U-

637 Th)/He thermochronometry. *Tectonics* 28, TC5009.
638 <https://doi.org/10.1029/2008TC002407>.

639 Gourbet, L., Leloup, P. H., Paquette, J.-L., Sorrel, P., Maheo, G., Wang, G.C., et al., 2017.
640 Reappraisal of the Jianchuan Cenozoic basin stratigraphy and its implications on the SE
641 Tibetan plateau evolution. *Tectonophysics* 700-701, 162–179.
642 <https://doi.org/10.1016/j.tecto.2017.02.007>.

643 Hoke, G.D., Liu-Zeng, J., Hren, M.T., Wissink, G.K., Garzzone, C.N., 2014. Stable isotopes
644 reveal high southeast Tibetan plateau margin since the Paleogene. *Earth and Planetary
645 Science Letters* 394, 270–278. <https://doi.org/10.1016/j.epsl.2014.03.007>.

646 Horton, B.K., Yin, A., Spurlin, M.S., Zhou, J., Wang, J., 2002, Paleocene–Eocene
647 syncontractional sedimentation in narrow, lacustrine-dominated basins of eastcentral
648 Tibet: *Geological Society of America Bulletin* 114 (7), 771–786.
649 [https://doi.org/10.1130/0016-7606\(2002\)114<0771:PESSIN>2.0.CO;2](https://doi.org/10.1130/0016-7606(2002)114<0771:PESSIN>2.0.CO;2).

650 Hu X.M., Garzanti, E., Wang, J.G., Huang, W.T., An, W., Webb, A., 2016. The timing of India-
651 Asia collision onset – Facts, theories, controversies. *Earth-Science Reviews* 160, 264-299.
652 <https://doi.org/10.1016/j.earscirev.2016.07.014>.

653 Kirby, E., Reiners, P. W., Krol, M. A., Whipple, K. X., Hodges, K. V., Farley, K. A., Chen, Z.,
654 2002. Late Cenozoic evolution of the eastern margin of the Tibetan Plateau: Inferences
655 from $^{40}\text{Ar}/^{39}\text{Ar}$ and (U–Th)/He thermochronology. *Tectonics* 21, 1001.
656 <https://doi.org/10.1029/2000TC001246>.

657 Leloup, P. H., Lacassin, R., Tapponnier, P., Scharer, U., Zhong, D.L., Liu, X.H., et al., 1995.
658 The Ailao Shan-Red River shear zone (Yunnan, China), Tertiary transform boundary of
659 Indochina. *Tectonophysics* 251(1–4), 3–84. [https://doi.org/10.1016/0040-1951\(95\)00070-](https://doi.org/10.1016/0040-1951(95)00070-4)
660 [4](https://doi.org/10.1016/0040-1951(95)00070-4).

661 Leloup, P.H., Arnaud, N., Lacassin, R., Kienast, J., Harrison, T., Trong, T.T.P., et al., 2001.
662 New constraints on the structure, thermochronology, and timing of the Ailao Shan-Red
663 River shear zone, SE Asia. *Journal of Geophysical Research* 106, 6683–6732.
664 <https://doi.org/10.1029/2000JB900322>.

665 Leloup, P. H., Tapponnier, P., Lacassin, R., 2007. Discussion on the role of the Red River shear
666 zone, Yunnan and Vietnam, in the continental extrusion of SE Asia. *Journal of the
667 Geological Society, London*, 164, 2007, pp. 1253–1260. [https://doi.org/10.1144/0016-](https://doi.org/10.1144/0016-76492007-065)
668 [76492007-065](https://doi.org/10.1144/0016-76492007-065).

669 Li, S.Y., Currie, B.S., Rowley, D.B., Ingalls, M., 2015. Cenozoic paleoaltimetry of the SE
670 margin of the Tibetan plateau: constraints on the tectonic evolution of the region. *Earth
671 and Planetary Science Letters* 432, 415–424. <https://doi.org/10.1016/j.epsl.2015.09.044>.

672 Liang, H.Y., Campbell, I.H., Allen, C.M., Sun, W.D., Yu, H.X., Xie, Y.W., Zhang, Y.-Q., 2007.
673 The age of the potassic alkaline igneous rocks along the Ailao Shan-Red River shear zone:
674 implications for the onset age of left-lateral shearing. *The Journal of Geology* 115, 231–
675 242. <https://doi.org/10.1086/527459>.

676 Lin, T. H., Lo, C. H., Chung, S. L., Hsu, F. J., Yeh, M. W., Lee, T. Y., et al., 2009. $^{40}\text{Ar}/^{39}\text{Ar}$
677 dating of the Jiali and Gaoligong shear zones: Implications for crustal deformation around
678 the eastern Himalayan syntaxis. *Journal of Asian Earth Sciences* 34(5), 674–685.
679 <https://doi.org/10.1016/j.jseas.2008.10.009>.

680 Liu-Zeng, J., Tapponnier, J.P., Gaudemer, Y., Ding, L., 2008. Quantifying landscape
681 differences across the Tibetan plateau: implications for topographic relief evolution.
682 *Journal of Geophysical Research* 113, F04018. <https://doi.org/10.1029/2007JF000897>.

683 Liu-Zeng, J., Zhang, J.Y., McPhillips, D., Reiners, P., Wang, W., Pik, R., et al., 2018. Multiple
684 episodes of fast exhumation since Cretaceous in southeast Tibet, revealed by low-
685 temperature thermochronology. *Earth and Planetary Science Letters* 490, 62–76.
686 <https://doi.org/10.1016/j.epsl.2018.03.011>.

687 Lu, Y. J., Kerrich, R., Cawood, P. A., McCuaig, T. C., Hart, C. J. R., Li, Z. X., et al. 2012.
688 Zircon SHRIMP U-Pb geochronology of potassic felsic intrusions in western Yunnan, SW
689 China: Constraints on the relationship of magmatism to the Jinsha suture. *Gondwana*
690 *Research* 22(2), 737–747. <https://doi.org/10.1016/j.gr.2011.11.016>.

691 Molnar, P., & Tapponnier, P., 1975. Cenozoic tectonics of Asia: effects of a continental
692 collision. *Science* 189, 419–426. <https://doi.org/10.1126/science.189.4201.419>.

693 Nie, J., Ruetenik, G., Gallagher, K., Hoke, G., Garzzone, C. N., Wang, W., et al. 2018. Rapid
694 incision of the Mekong River in the middle Miocene linked to monsoonal precipitation.
695 *Nature Geoscience* 11(12), 944–948. <https://doi.org/10.1038/s41561-018-0244-z>.

696 Ouimet, W., Whipple, K., Royden, L., Reiners, P., Hodges, K., Pringle, M., 2010. Regional
697 incision of the eastern margin of the Tibetan plateau. *Lithosphere* 2, 50.
698 <https://doi.org/10.1130/L57.1>.

699 Perrineau, A., 2010. Evolution morphologique et tectonique récente des marges NE et SE du
700 plateau tibétain: Lien avec la dynamique des grands fleuves. Institut de Physique du Globe
701 de Paris. pp. 421.

702 Reiners, P. W., & Brandon, M. T., 2006. Using thermochronology to understand orogenic
703 erosion. *Annual Review of Earth and Planetary Sciences* 34(1), 419–466.
704 <https://doi.org/10.1146/annurev.earth.34.031405.125202>.

705 Replumaz, A., Lacassin, R., Tapponnier, P., Leloup, P. H., 2001. Large river offsets and Plio-
706 Quaternary dextral slip rate on the Red River fault (Yunnan, China). *Journal of*
707 *Geophysical Research* 106(B1), 819–836. <https://doi.org/10.1029/2000JB900135>.

708 Roger, F., J. Malavieille, P. H. Leloup, S. Calassou, Z. Xu, 2004. Timing of granite
709 emplacement and cooling in the Songpan-Garze Fold Belt (eastern Tibetan Plateau) with
710 tectonic implications. *Journal of Asian Earth Sciences* 22(5), 465–481.
711 [https://doi.org/10.1016/S0137-9120\(03\)00089-0](https://doi.org/10.1016/S0137-9120(03)00089-0).

712 Roger, F., Jolivet, M. Malavieille, J., 2010. The tectonic evolution of the Songpan Garze
713 (North Tibet). *Journal of Asian Earth Sciences* 39, 254–269.
714 <https://doi.org/10.1016/j.crte.2007.10.014>.

715 Royden, L. H., Burchfiel, B. C., King, R. W., Wang, E., Zhiliang, C., Feng, S., Yuping, L.,
716 1997. Surface deformation and lower crustal flow in eastern Tibet. *Science* 276(5313),
717 788–790. <https://doi.org/10.1126/science.276.5313.788>.

718 Schärer, U., Zhang, L. S., Tapponnier, P., 1994. Duration of strike-slip movements in large
719 shear zones: The Red River belt, China. *Earth and Planetary Science Letters* 126(4), 379–
720 397. [https://doi.org/10.1016/0012-821X\(94\)90119-8](https://doi.org/10.1016/0012-821X(94)90119-8).

721 Schildgen, T.F., & van der Beek, P.A., 2019. The Application of Low-Temperature
722 Thermochronology to the Geomorphology of Orogenic Systems. In M. G. Malusà and P.
723 G. Fitzgerald (Eds.), *Fission-Track Thermochronology and its Application to Geology* (pp.
724 335-350). Springer Textbooks in Earth Sciences, Geography and Environment.

725 Schoenbohm, L.M., Burchfiel, B.C., Chen, L., 2006. Propagation of surface uplift, lower
726 crustal flow, and Cenozoic tectonics of the southeast margin of the Tibetan plateau.
727 *Geology* 34, 813–816. <https://doi.org/10.1130/G22679.1>.

728 Shen, T.Y., Wang G.C., Leloup, P. H., van der Beek, P., Bernet, M., Cao, K., Wang, A., Liu,
729 C., Zhang K.X., 2016a. Controls on Cenozoic exhumation of the Tethyan Himalaya from
730 fission-track thermochronology and detrital zircon U-Pb geochronology in the Gyirong
731 basin area, southern Tibet, *Tectonics* 35, 1713-1734. <https://doi:10.1002/2016TC004149>.

732 Shen, X.M., Tian, Y.T., Li, D.W., Qin, S.W., Vermeesch, P., Schwanethal, J., 2016b.
733 Oligocene-Early Miocene river incision near the first bend of the Yangze River: Insights
734 from apatite (U-Th-Sm)/He thermochronology. *Tectonophysics* 687, 223–231.
735 <https://doi.org/10.1016/j.tecto.2016.08.006>.

736 Shuster, D. L., Flowers, R. M. Farley, K. A., 2006. The influence of natural radiation damage
737 on helium diffusion kinetics in apatite. *Earth and Planetary Science Letters* 249, 148-161.
738 <https://doi.org/10.1016/j.epsl.2006.07.028>.

739 Si, G., Li, Y., & Hou, Z., 2000, The Tertiary stratigraphy sequence of Yanyuan Basin in the
740 southeastern margin of the Qinghai-Tibet Plateau, *Earth Science Frontiers*, 7, 304–305.

741 Spurlin, M.S., Yin, A., Horton, B.K., Zhou, J., Wang, J., 2005, Structural evolution of the
742 Yushu-Nangqian region and its relationship to syncollisional igneous activity, east-central
743 Tibet. *Geological Society of America Bulletin* 117 (9–10), 1293–1317.
744 <https://doi.org/10.1130/B25572.1>.

745 Staisch, L.M., Niemi, N.A., Clark, M.K., Chang, H., 2016, Eocene to late Oligocene history of
746 crustal shortening within the Hoh Xil Basin and implications for the uplift history of the
747 northern Tibetan Plateau. *Tectonics* 35 (4), 862–895.
748 <https://doi.org/10.1002/2015TC003972>.

749 Su, T., Spicer, R.A., Li, S.H., Xu, H., Huang, J., Sherlock, S., Huang, Y.J., Li, S.F. et al., 2018.
750 Uplift, climate and biotic changes at the Eocene–Oligocene transition in south-eastern
751 Tibet. *National Science Review* 6(3), 495–504. <https://doi.org/10.1093/nsr/nwy062>.

752 Tang, M.Y., Liu-Zeng, J., Hoke, G. D., Xu, Q., Wang, W.T., Li, Z.F., et al., 2017.
753 Paleoelevation reconstruction of the Paleocene-Eocene Gonjo basin, SE-central Tibet.
754 *Tectonophysics* 712-713, 170–181. <https://doi.org/10.1016/j.tecto.2017.05.018>.

755 Tapponnier, P., Zhiqin, X., Roger, F., Meyer, B., Arnaud, N., Wittlinger, G., Jingsui, Y., 2001.
756 Oblique stepwise rise and growth of the Tibet plateau. *Science* 294(5547), 1671–1677.
757 <https://doi.org/10.1126/science.105978>.

758 Tian, Y.T., Kohn, B.P., Gleadow, A.J., Hu, S.B., 2013. Constructing the Longmen Shan eastern
759 Tibetan plateau margin: insights from low-temperature thermochronology. *Tectonics* 32,
760 576–592. <https://doi.org/10.1002/tect.20043>.

761 Tian, Y.T., Kohn, B.P., Gleadow, A.J.W., Hu, S.B., 2014. A thermochronological perspective
762 on the morphotectonic evolution of the southeastern Tibetan plateau. *Journal of*
763 *Geophysical Research* 119, 676–698. <https://doi.org/10.1002/2013JB010429>.

764 Vermeesch, P., Seward D., Latkoczt, C., Wipf, M., Gunther D., Baur, H., 2007. Alpha-emitting
765 mineral inclusions in apatite, their effect on (U-Th)/He ages, and how to reduce it.
766 *Geochimica et Cosmochimica Acta* 71, 1737-1746.
767 <https://doi.org/10.1016/j.gca.2006.09.020>.

768 Vermeesch, P., & Tian, Y. T., 2014. Thermal history modelling: HeFTy vs. QTQt. *Eart-Science*
769 *Reviews* 139, 279–290. <https://doi.org/10.1016/j.earscirev.2014.09.010>.

770 Wagner G., & van den Haute P., 1992. Fission-track dating. Kluwer Academic Publishers,
771 Dordrecht, Solid Earth Sciences Library. pp. 285.

772 Wallis, S., Tsujimori, T., Aoya, M., Kawakami, T., Terada, T., Suzuki, K., Hyodo, H., 2003.
773 Cenozoic and Mesozoic metamorphism in the Longmenshan orogen: Implications for
774 geodynamic models of eastern Tibet. *Geology* 31 (9), 745–748.
775 <https://doi.org/10.1130/G19562.1>.

776 Wang, E., Burchfiel, B.C., Royden, L.H., Chen, L., Chen, J., Li, W., Chen, Z., 1998. The
777 Cenozoic Xianshuihe–Xiaojiang, Red River, and Dali Fault Systems of southwestern
778 Sichuan and central Yunnan, China. *Spec. Pap., Geological Society of America Bulletin*
779 327. 108 <https://doi.org/10.1130/0-8137-2327-2.1>.

780 Wang, E., & Burchfiel, B.C., 2000. Late Cenozoic to Holocene deformation in southwestern
781 Sichuan and adjacent Yunnan, China, and its role in formation of the southeastern part of
782 the Tibetan Plateau. *Geological Society of America Bulletin* 112, 413–423.
783 [https://doi.org/10.1130/0016-7606\(2000\)112<413:LCTHDI>2.0.CO;2](https://doi.org/10.1130/0016-7606(2000)112<413:LCTHDI>2.0.CO;2).

784 Wang, E., Kirby, E., Furlong, K., van Soest, M., Xu, G., Shi, X., Kamp, P., Hodges, K., 2012a.
785 Two-phase growth of high topography in eastern Tibet during the Cenozoic. *Nature*.
786 *Geoscience* 5, 640–645. <https://doi.org/10.1038/ngeo1538>.

787 Wang, G.C., Zhang, K.X., Xiang, S.Y., Wang, A., Cao, K. et al., 2014. Cenozoic geological
788 map and guidebook of Tibet Plateau and its adjacent regions 1:1 500 000, 2014. China
789 University of Geosciences Press, Wuhan, pp. 155.

790 Wang, H., Tian, Y., Liang, M., 2017. Late Cenozoic exhumation history of the Luoji Shan in
791 the southeastern Tibetan Plateau: Insights from apatite fission-track thermochronology.
792 *Journal of the Geological Society* 174, 883-891. <https://doi.org/10.1144/jgs2017-005>.

793 Wang, S.F., Fang, X.M., Zheng, D.W., Wang, E., 2009. Initiation of slip along the Xianshuihe
794 fault zone, eastern Tibet, constrained by K/Ar and fission-track ages. *International*
795 *Geology Review* 51(12), 1121–1131. <https://doi.org/10.1080/00206810902945132>.

796 Wang, S.F., Jiang, G.G., Xu, T.D., Tian, Y.T., Zheng, D.W., Fang, X.M., 2012b. The Jinhe-
797 Qinghe fault—An inactive branch of the Xianshuihe-Xiaojiang fault zone, eastern Tibet.
798 *Tectonophysics* 544-545, 93–102. <https://doi.org/10.1016/j.tecto.2012.04.004>.

799 Wang, Y., Zhang, B., Schoenbohm, L.M., Zhang, J., Zhou, R., Hou, J., Ai, S., 2016. Late
800 Cenozoic tectonic evolution of the Ailao Shan-Red River fault (SE Tibet): Implications
801 for kinematic change during plateau growth, *Tectonics* 35, 1969–1988,
802 <http://doi:10.1002/2016TC004229>.

803 Wu G.L., Zhu C.Y., Wang G.C., Zhang P., 2019. Demarcation of the geomorphological
804 boundaries of southeastern Tibet: implications for expansion mechanisms of the plateau
805 edge. *Seismology and Geology* 2(41), 281-299 (in Chinese with English abstract). <http://doi.org/10.3969/j.issn.0253-4967.2019.02.003>.

807 Wu, J., Zhang, K., Xu, Y., Wang, G., Garzzone, C. N., Eiler, J., Leloup, P. H., et al., 2018,
808 Paleoelevations in the Jianchuan Basin of the southeastern Tibetan Plateau based on stable
809 isotope and pollen grain analyses. *Palaeogeography, Palaeoclimatology, Palaeoecology*
810 510, 93-108. <https://doi.org/10.1016/j.palaeo.2018.03.030>.

811 Xu, G., & Kamp, P. J. J., 2000. Tectonics and denudation adjacent to the Xianshuihe fault,
812 eastern Tibetan plateau: Constraints from fission track thermochronology. *Journal of*
813 *Geophysical Research* 105(B8), 19,231–19,251. <https://doi.org/10.1029/2000JB900159>.

814 Yan, B., & Lin, A., 2015. Systematic deflection and offset of the Yangtze River drainage system
815 along the strike-slip Ganzi–Yushu–Xianshuihe fault zone, Tibetan Plateau. *Journal of*
816 *Geodynamics* 87, 13–25. <http://doi/10.1016/j.jog.2015.03.002>.

817 Yang, R., Fellin, M.G., Herman, F., Willett, S.D., Wang, W., Maden, C., 2016. Spatial and
818 temporal pattern of erosion in the three rivers region, southeastern Tibet. *Earth and*
819 *Planetary Science Letters* 433, 10–20. <https://doi.org/10.1016/j.epsl.2015.10.032>.

820 Zachos, J., Pagani, M., Sloan, L., Thomas, E., Billups, K., 2001. Trends, rhythms, and
821 aberrations in global climate 65 Ma to present. *Science* 292, 686–693.
822 <https://doi.org/10.1126/science.1059412>.

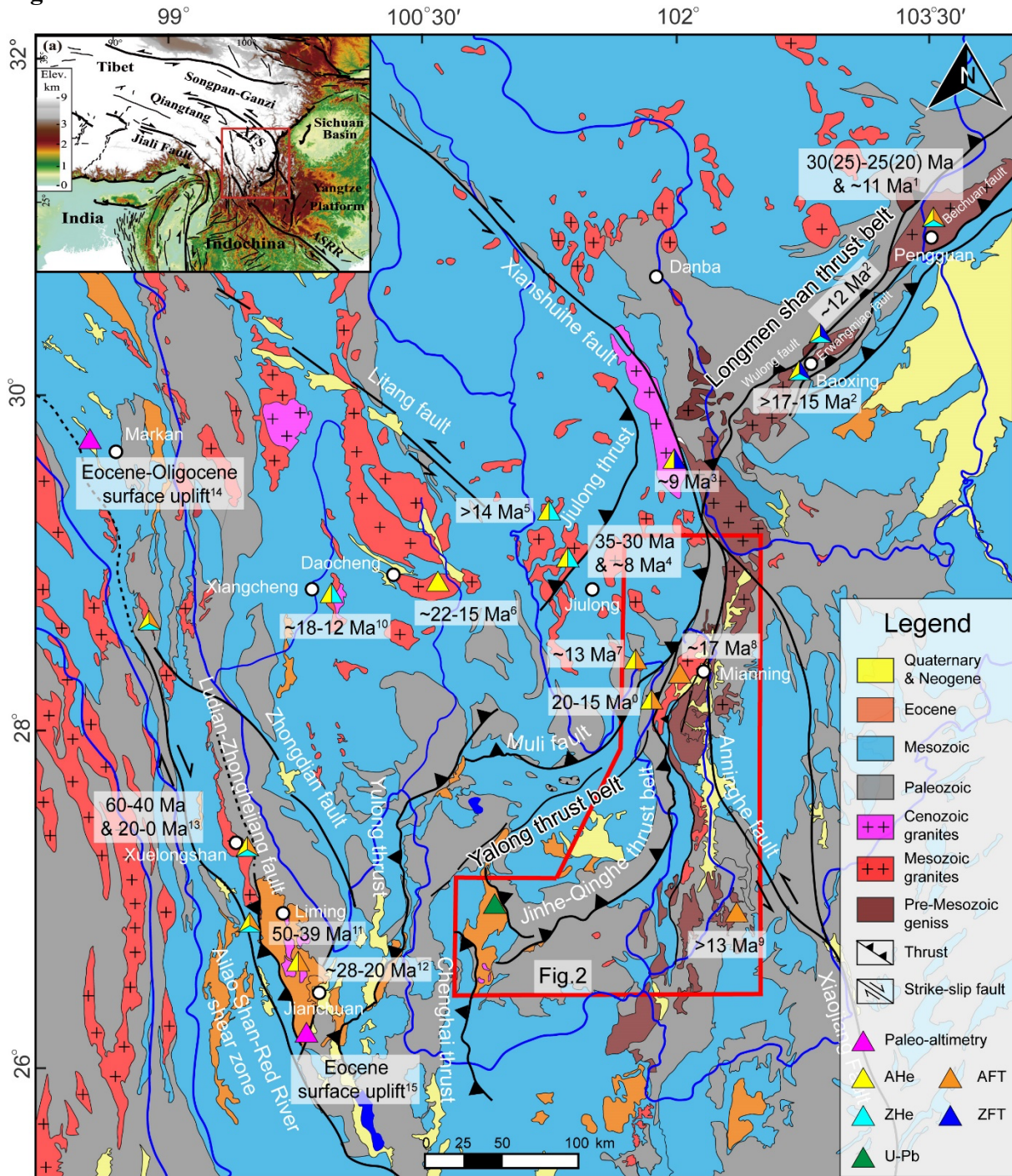
823 Zhang, B., Zhang, J.J., Chang, Z.F., Wang, X.X., Cai, F.L., Lai, Q.Z., 2012. The Biluoxueshan
824 transpressive deformation zone monitored by synkinematic plutons, around the eastern
825 Himalayan syntaxis. *Tectonophysics* 574-575, 158–180.
826 <https://doi.org/10.1016/j.tecto.2012.08.017>.

827 Zhang, H.P., Oskin, M. E., Liu-Zeng, J., Zhang, P.Z., Reiners, P. W., Xiao, P., 2016. Pulsed
828 exhumation of interior eastern Tibet: Implications for relief generation mechanisms and
829 the origin of high-elevation planation surfaces. *Earth and Planetary Science Letters* 449,
830 176–185. <https://doi.org/10.1016/j.epsl.2016.05.048>.

- 831 Zhang, P. Z., Shen, Z., Wang, M., Gan, W. J., Burgmann, R., Molnar, P., et al., 2004.
832 Continuous deformation of the Tibetan Plateau from global positioning system data.
833 *Geology* 32(9), 809–812. <https://doi.org/10.1130/G20554.1>.
- 834 Zhang, Y. Z., Replumaz, A., Wang, G. C., Leloup, P. H., Gautheron, C., Bernet, M., et al.,
835 2015. Timing and rate of exhumation along the Litang fault system, implication for fault
836 reorganization in southeast Tibet. *Tectonics* 34, 1219–1243.
837 <https://doi.org/10.1002/2014TC003671>.
- 838 Zhang, Y. Z., Replumaz, A., Leloup, P. H., Wang, G. C., Bernet, M., van der Beek, P., et al.,
839 2017. Cooling history of the Gongga batholith: Implications for the Xianshuihe fault and
840 Miocene kinematics of SE Tibet. *Earth and Planetary Science Letters* 465, 1–15.
841 <https://doi.org/10.1016/j.epsl.2017.02.025>.
- 842 Zheng, H. B., Clift, P. D., He, M. Y., Bian, Z. X., Liu, G. Z., Liu, X. C., Xia L., et al., 2020.
843 Formation of the First Bend in the late Eocene gave birth to the modern Yangtze River,
844 China. *Geology* 48. <https://doi.org/10.1130/G48149.1>.

1 **Figures (1-11)**

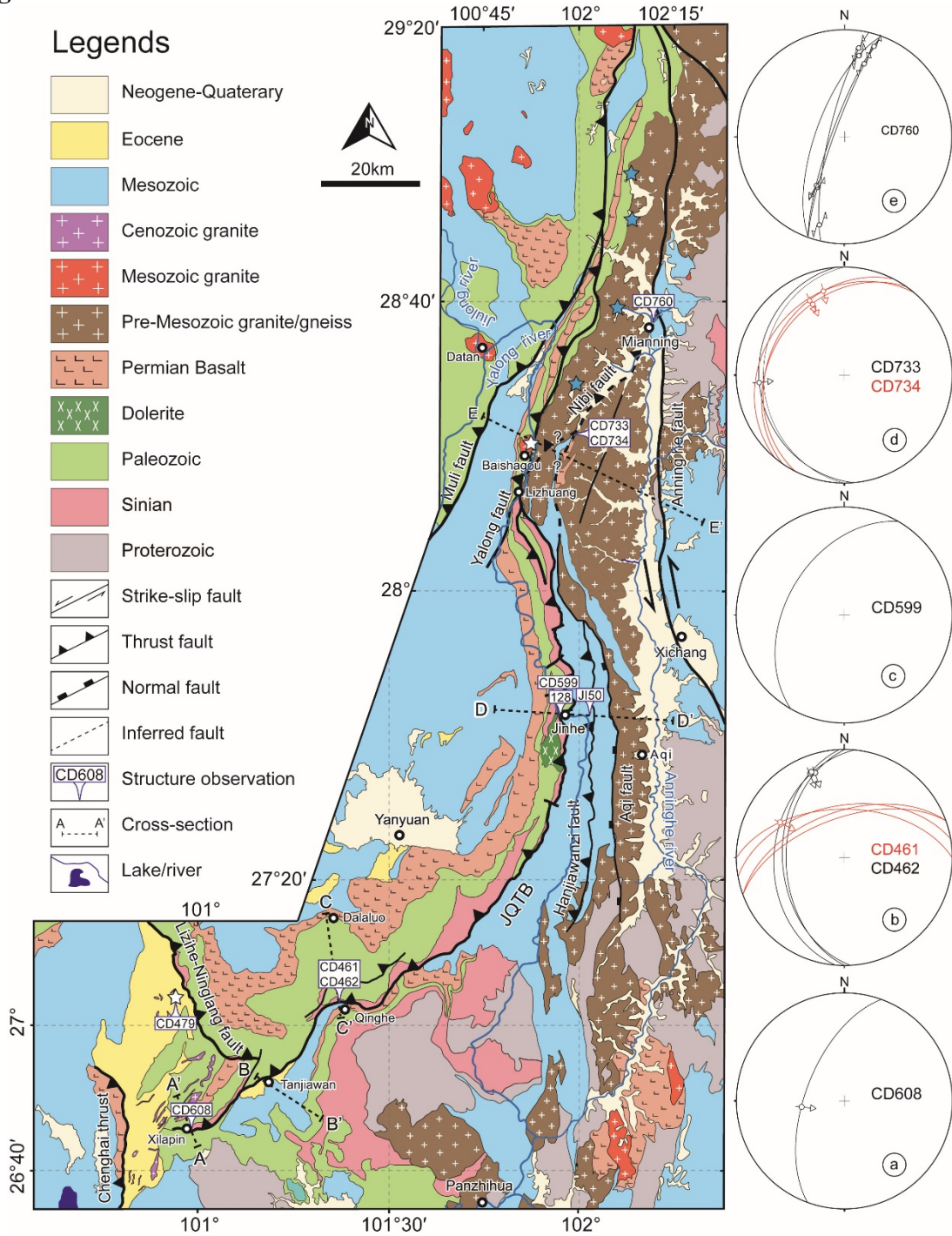
2 **Figure 1**



3
4 Fig. 1. Simplified geology and topography of southeastern Tibet, with major faults (modified
5 after Leloup et al., 1995; Zhang et al., 2017; Cao et al., 2019). The inset in the upper left corner
6 shows the location of southeastern Tibet. The triangle symbols denote accelerated exhumation
7 phases derived from low-temperature thermochronology in southeastern Tibet: 0 = This study,
8 1 = E. Wang et al. (2012), 2 = Cook et al. (2013), 3 = Zhang et al. (2017), 4 = Zhang et al.
9 (2016), 5 = Ouimet et al. (2010), 6 = Tian et al. (2014), 7 = Clark et al. (2005), 8 = S. Wang et
10 al. (2012), 9 = Wang et al. (2017), 10 = Gourbet et al. (2020), 11 = Cao et al. (2020), 12 = Cao
11 et al. (2019), 13 = Liu et al. (2018), 14 = Su et al. (2018), 15 = Hoke et al. (2014).

12

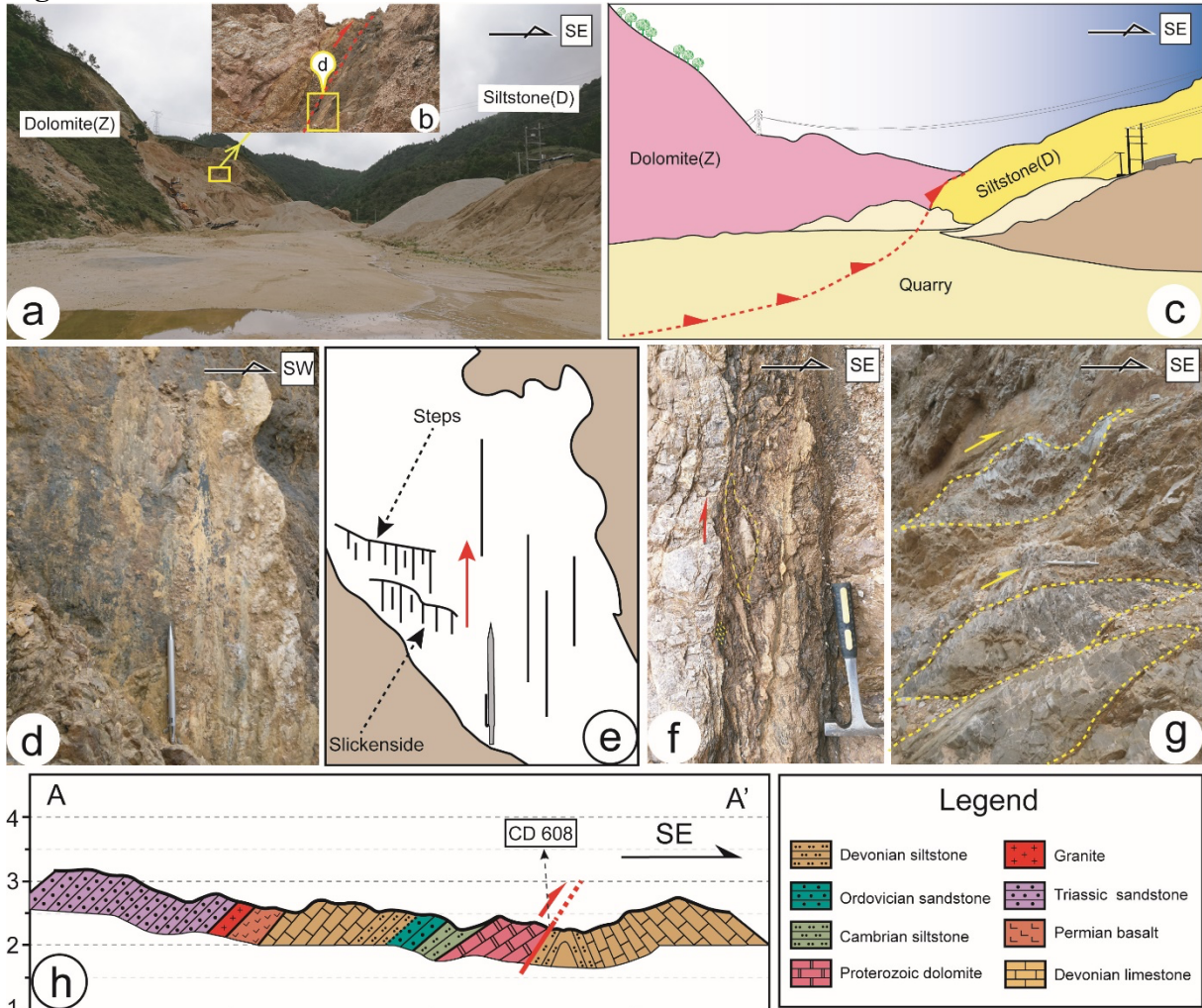
13 **Figure 2**



14

15 Fig. 2. Geological map of the Jinhe-Qinghe Thrust Belt based on BGMR Yunnan (1990),
 16 BGMR Sichuan (1991), S. Wang et al. (2012), and our new field observations. See Figure 1 for
 17 the location. A-e are the stereoplots shown of the Jinhe-Qinghe thrust belt at sites CD608,
 18 CD461 and CD462, CD598, CD733 and CD734, CD760, and CD759, from south to north,
 19 respectively. The locations of cross-sections A-A', B-B', C-C', D-D', E-E', and corresponding
 20 outcrops pictures are provided in Figures 3-7. The blue star denotes the AFT samples' locations
 21 in S. Wang et al. (2012). The white stars denote the sample locations in this study.

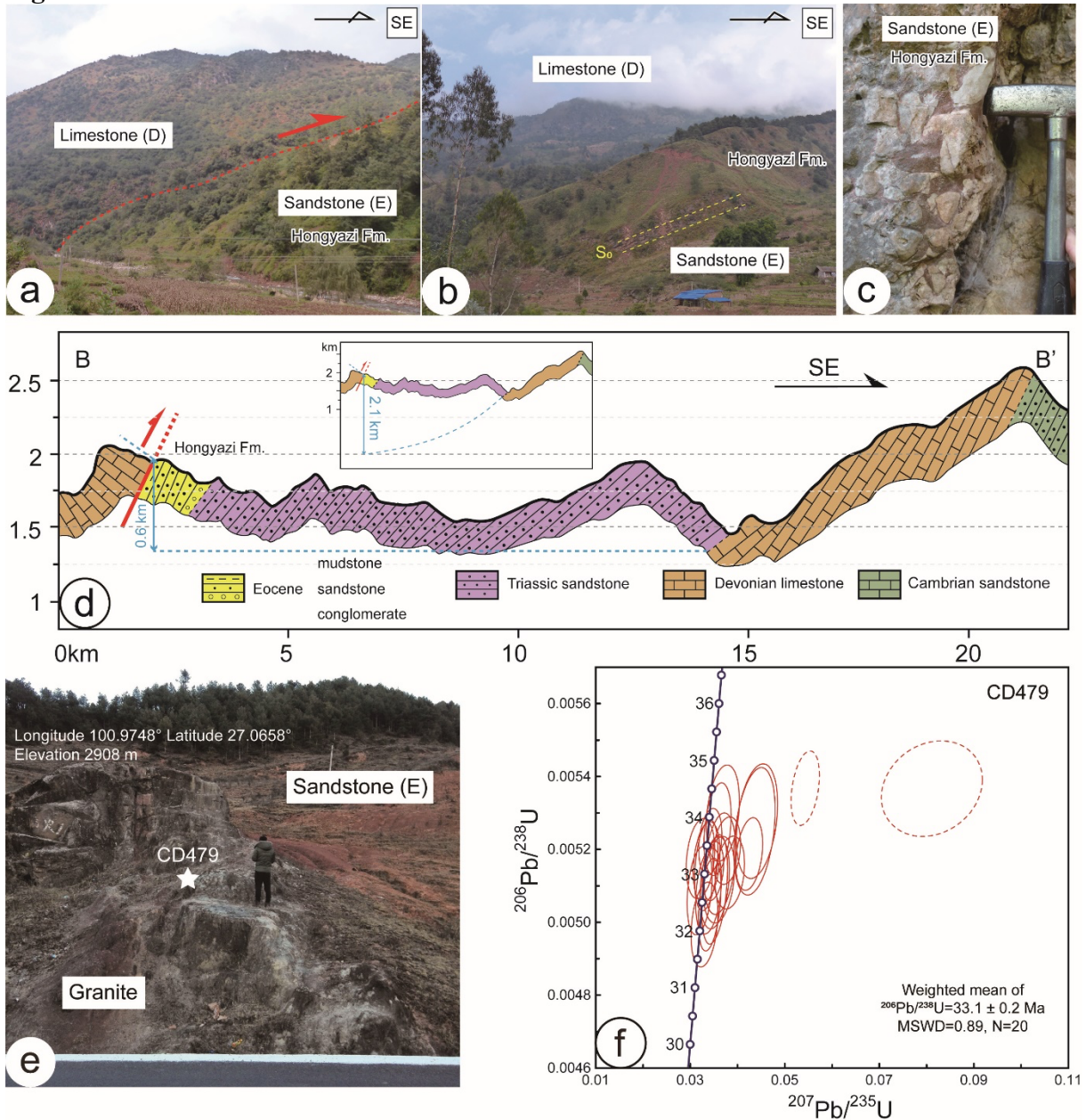
22 **Figure 3**



23
 24 Fig. 3 Field observations in the Xilaping area. (a) Site CD608 picture with Sinian (Z) dolomite
 25 on the left and Devonian (D) sediments on the right. (b) Damage zone in the dolomite. (c)
 26 Sketch corresponding to Figure 3a. (d) Close up of the fault plane with slickensides indicating
 27 thrust motion (see location in Figure 3b). (e) Sketch corresponding to Figure 3e. (f) and (g)
 28 Asymmetric dolomitic lenses compatible with the reverse motion of the JQTB. (h) Cross-
 29 section in the Xilaping area perpendicular to the strike of the fault. See Figure 2 for location.
 30 Vertical exaggeration is 2x.

31

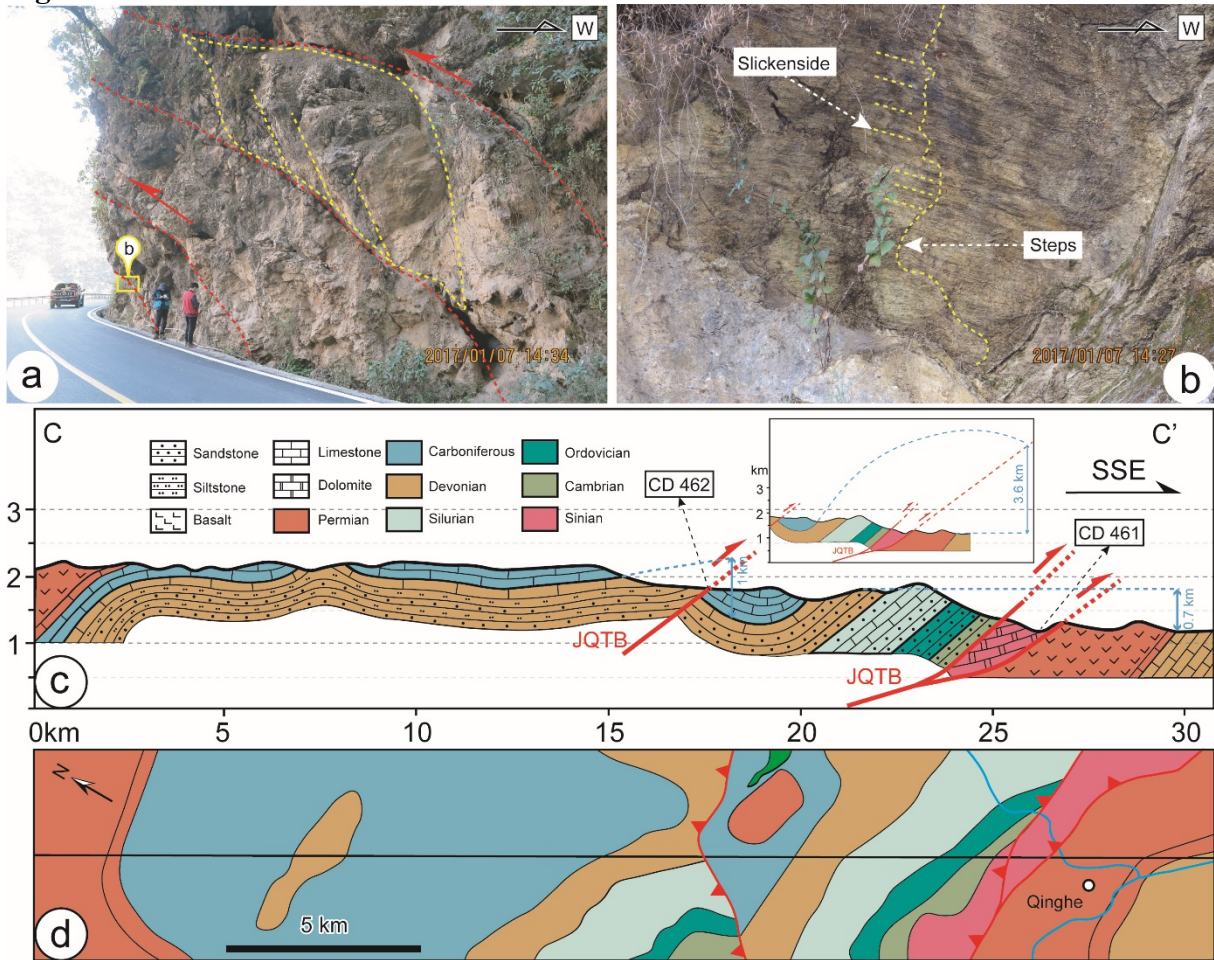
32 **Figure 4**



33
 34 Fig. 4 Field observations in Tanjiawan and Ninglang. (a, b) Landscape pictures of the NW
 35 boundary of the Tanjiawan Basin showing the Devonian limestone thrust on top of the
 36 Eocene sandstone. (c) Conglomerates with limestone pebbles at the bottom of the Hongyazi
 37 Fm. (d) Cross-section across the Tanjiawan Eocene basin. See Figure 2 for location. Vertical
 38 exaggeration is 3x. Inset: estimate of the maximum apparent vertical offset. (e) Picture of site
 39 CD479 where granite is intrusive into sediments (Ninglang Fm.). (f) Concordia plot of Zircon
 40 U-Pb data of the granite intrusion shown in (e) (sample CD479).

41

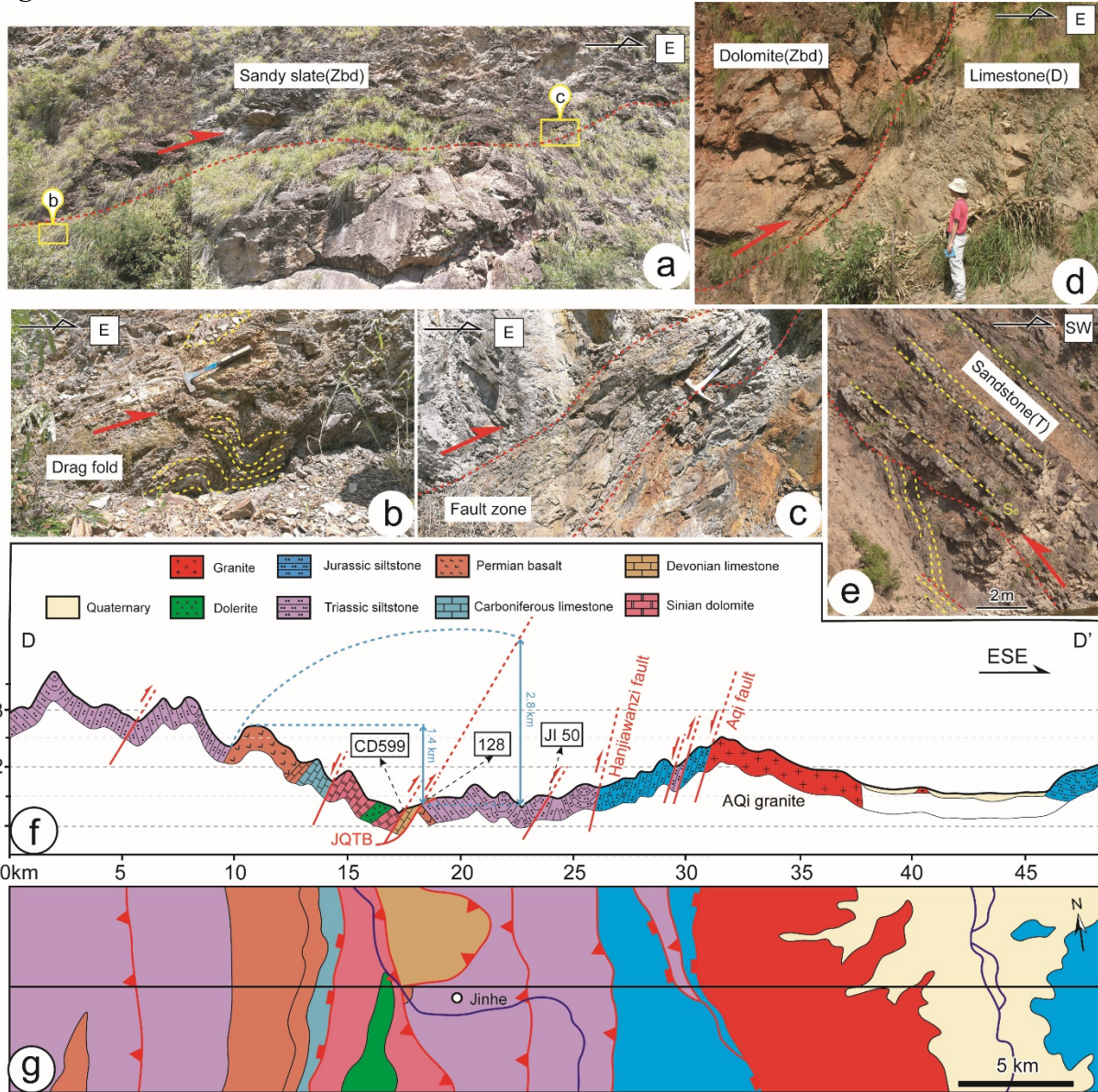
42 **Figure 5**



43
 44 Fig. 5 Field observations along the Qinghe-Dalaluo cross-section. (a) Outcrop of a series of
 45 minor faults at site CD462. (b) Slickensides and steps developed in the Devonian limestone. (c)
 46 Qinghe-Dalaluo cross-section. See Figure 2 and 5d for location. Vertical exaggeration is 2x.
 47 Inset: estimate of the maximum apparent vertical offset. (d) Geological map of the Qinghe-
 48 Dalaluo cross-section. Black line is Fig. 5c cross-section trace. Mapping is based on Geol. map
 49 G47-12 and this study.

50

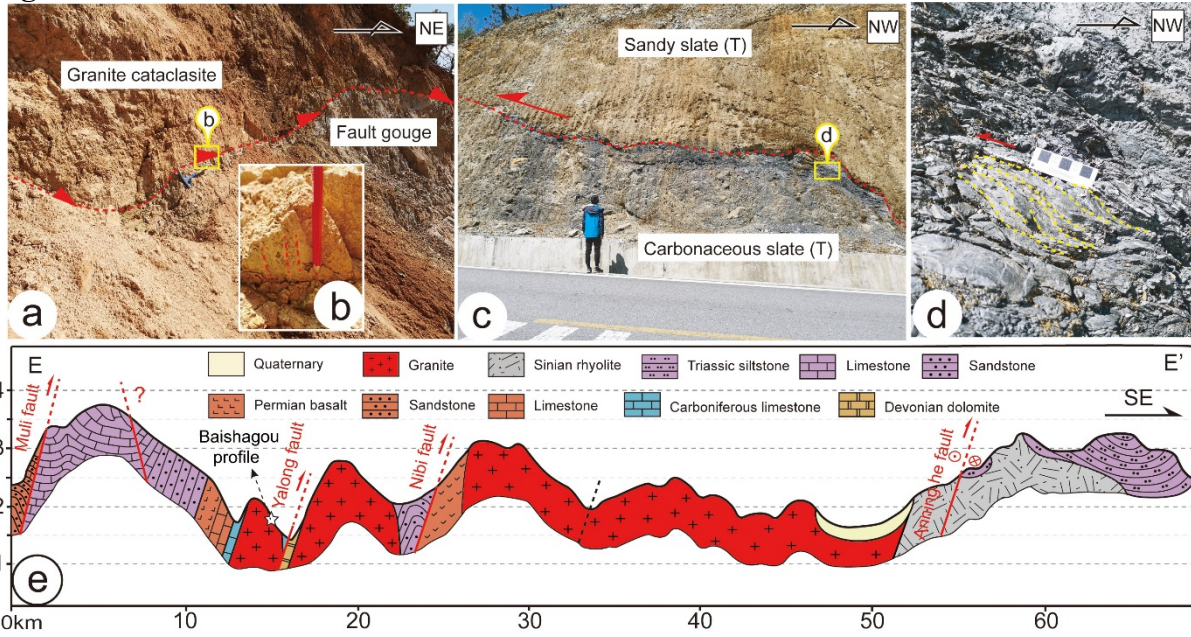
51 **Figure 6**



52
 53 Fig. 6 Field observations along the Jinhe cross-section. (a)-(c) Outcrops of the fault zone
 54 showing drag fault in Sinian dolomite near the Jinhe bridge (site CD599). (d) site 128. Outcrop
 55 of Sinian (Zbd and gabbros) thrust above Upper Permian basalts. (e) Thrust fault within
 56 Triassic siltstones at site JI50. (f) Jinhe cross-section. See Figure 2 and 6g for location. Vertical
 57 exaggeration is 2x. (g) Geological map of the Jinhe cross-section. Black line is Fig. 6f cross-
 58 section trace. Mapping is based on Geol. map G47-06 and this study.

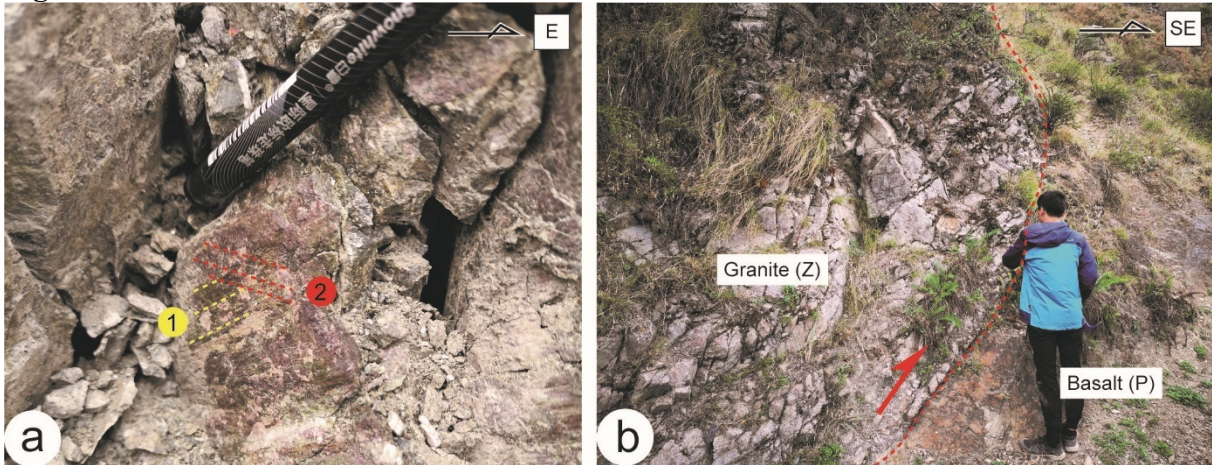
59

60 **Figure 7**



61
 62 Fig. 7 Field observations along the Mianning–Yalong section. (a-b) site CD733. Cataclastic
 63 granite. (b) Fault plane striking N355° 52°W with slickensides trending N339°. (c-d) Site
 64 CD733b showing thrusting of granite on top of Triassic slate. (d) Triassic sediments are strongly
 65 schistosed with slickenside trending N335°. (e-f) CD734 Outcrop of the contact between sandy
 66 slate and carbonaceous slate at the site. (f) S-C fabrics in carbonaceous slate near the structure
 67 contact. (i) Mianning-Yalong cross-section. See Figure 2 for the location. Vertical exaggeration
 68 is 3x.
 69

70 **Figure 8**

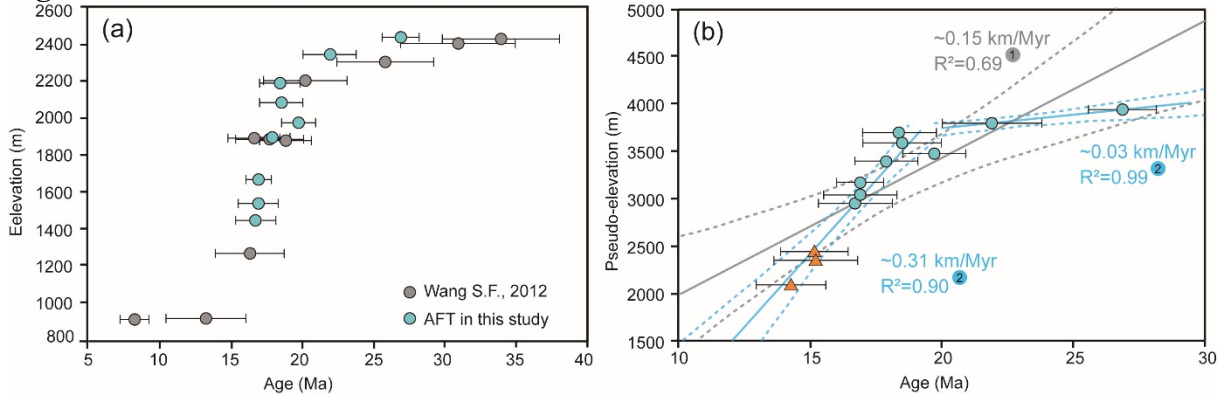


71

72 Fig. 8 Field observations around the Mianning area of site CD760. (a) two groups of
73 slickensides on the fault plane. Fault plane striking $N20^{\circ} 80^{\circ}W$ with slickensides trending
74 $N350^{\circ}$ cut by another one trending $N215^{\circ}$. (b) Structural contact between Sinian granite and
75 Permian basalt at site CD760.

76

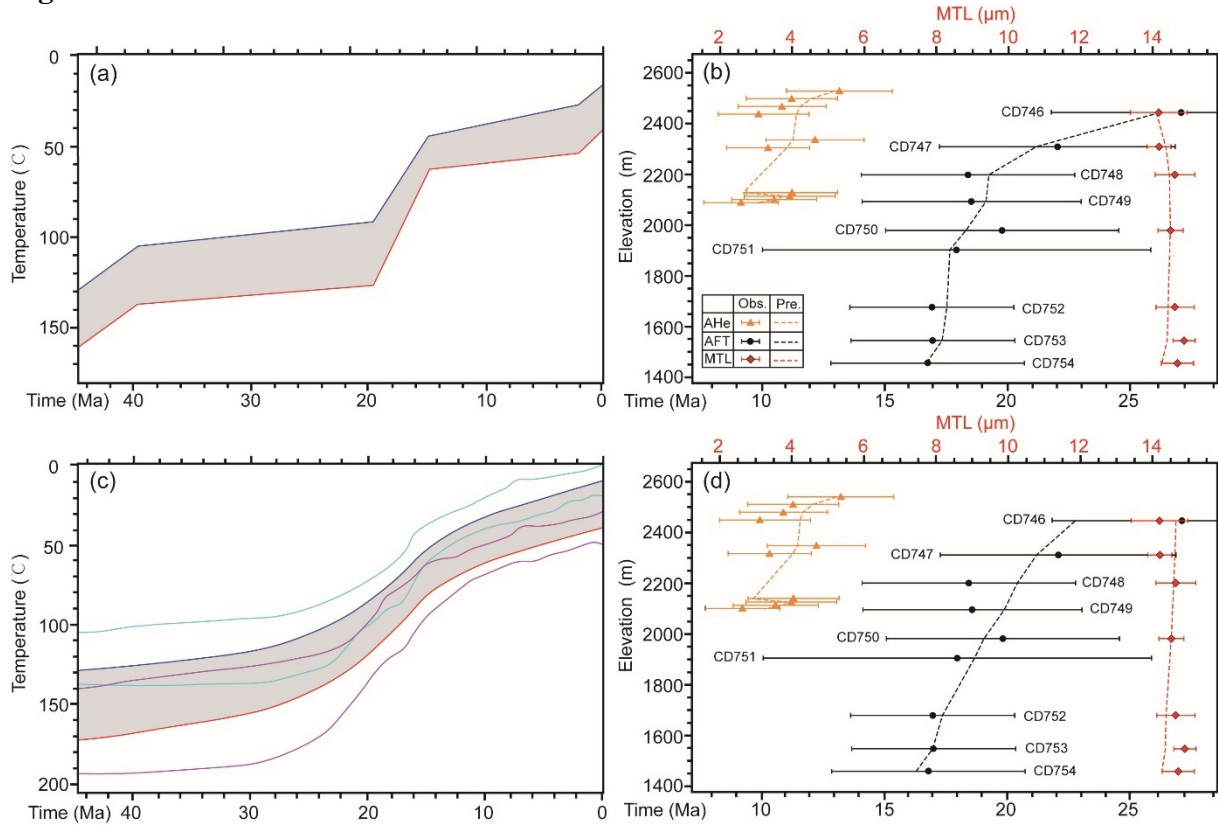
77 **Figure 9**



78

79 Fig. 9 AFT and AHe age elevation relationships (a) AFT age vs elevation plot. Data from S.
 80 Wang et al., (2012) and this study. (b) AFT and AHe age vs pseudo-elevation profile (see text
 81 for details). Data from this study. Two fits to the data are proposed: a single linear regression
 82 array corresponding to a stable exhumation history, presented by gray lines (model 1); and two
 83 arrays with a break in slope at ~19 Ma corresponding to two exhumation episodes model,
 84 presented by blue lines (model 2). The solid lines are the least-squares regression relationships
 85 of the samples, and the dashed lines represent the 95% confidence intervals.

86 **Figure 10**

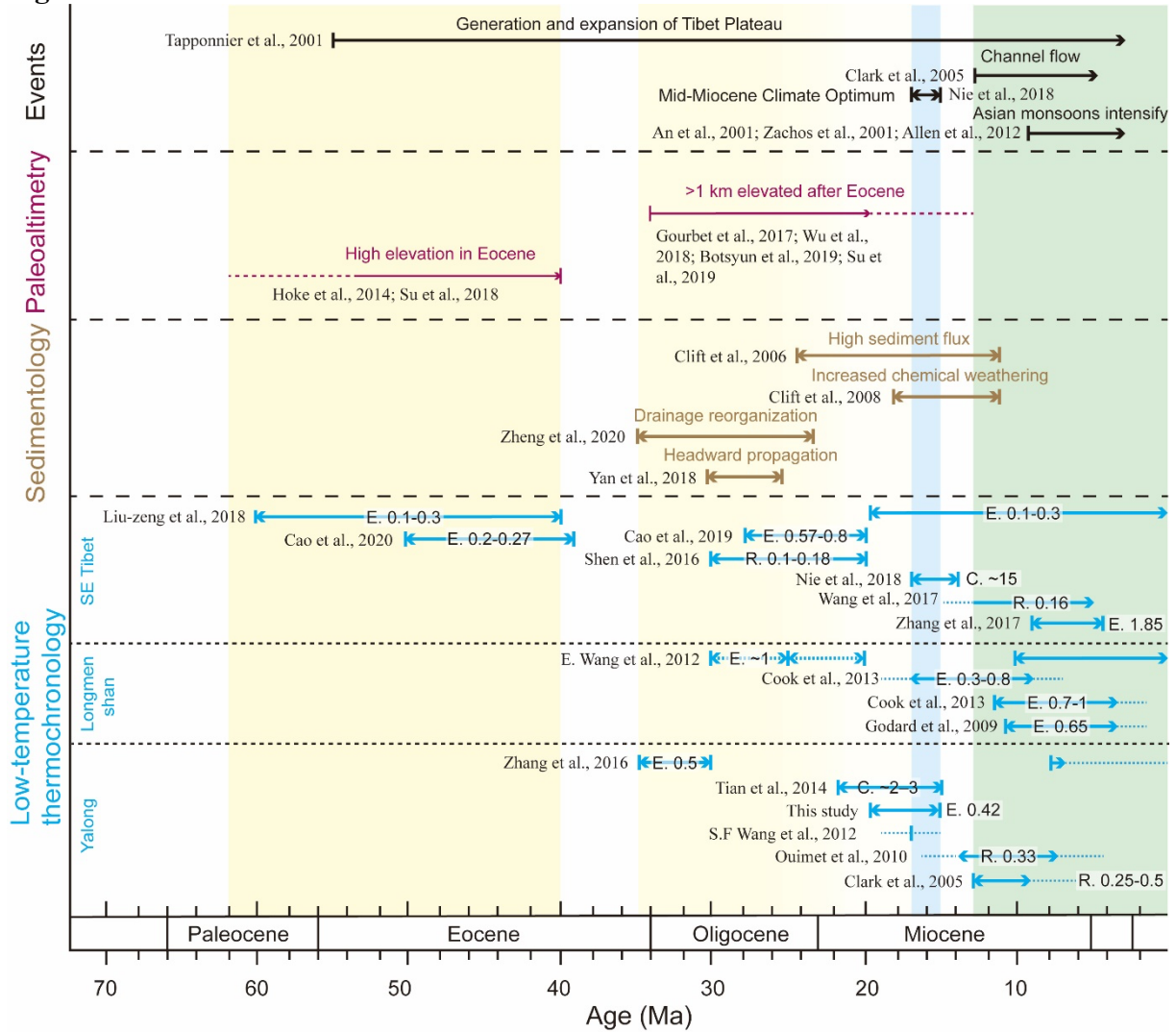


87

88 Fig. 10 Cooling history of the Baishagou vertical profile based on QTQt inverse modeling. (a)
 89 and (c) Cooling history derived from the maximum likelihood model and the expected model,
 90 respectively. (b) and (d) Comparison between the observed and predicted values for all samples
 91 in the profile (single-grain ages for AHe and central ages for AFT). For the highest elevation
 92 sample, the thermal history is plotted by the blue curve and the 95% credible intervals are drawn
 93 in cyan. For the lowest elevation sample, the thermal history is plotted by the red curve and the
 94 95% credible intervals are drawn in magenta. Intermediate sample thermal histories are shown
 95 in the grey area. MTL=mean track length

96

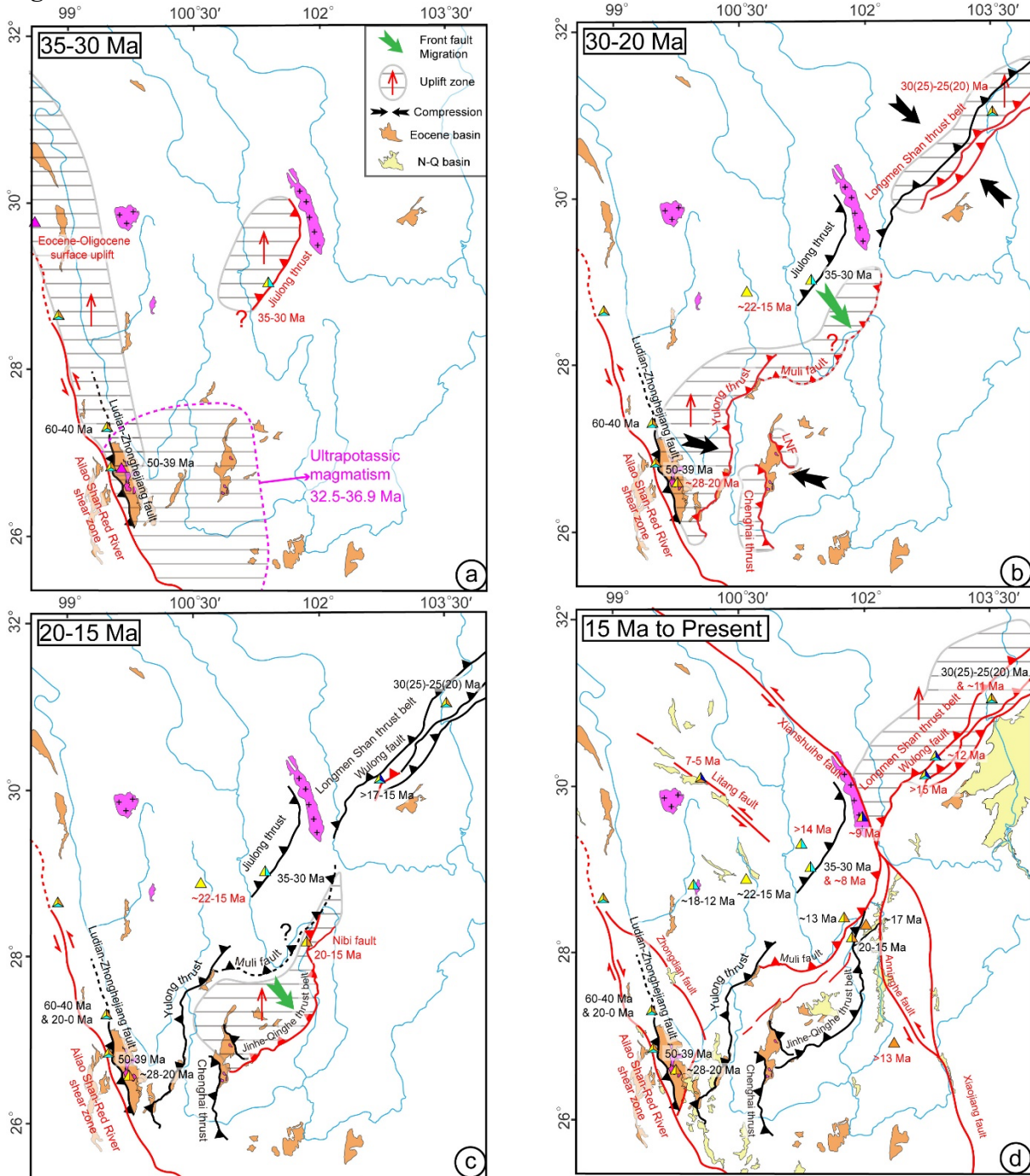
97 **Figure 11**



98

99 Fig. 11 Regional compilation of fast cooling/exhumation events with respect to paleo-altimetry
 100 and sediment flux in the South China Sea. Low-temperature thermochronology studies are
 101 derived from age-elevation profiles (see Figure 1 for localization) in southeastern Tibet. E. =
 102 exhumation rate, km/Myr; R. =river incision rate, km/Myr; C. =cooling rate, °C/Myr. The
 103 yellow zones indicate the uplift events resulting from the southeast extrusion of Tibetan Plateau
 104 and its corresponding fast exhumation, sedimentary records and increase in paleo-elevation.
 105 The blue rectangle indicates the Mid-Miocene climate optimum. The green rectangle indicates
 106 Late Miocene river incision which has been interpreted as due to lower crustal flow.

107



109

110 Fig. 12 Late Eocene to present evolution of the southeastern Tibetan Plateau during the
 111 southeastward extrusion of Indochina. The differential exhumation resulting from thrusting
 112 along thrust belts are responsible for relief generation during the Oligocene to Early Miocene
 113 (see details in discussion). N-Q: Neogene-Quaternary. The rivers and the faults are marked in
 114 their present-day shape and locations. The red line and text indicate the faults were active during
 115 this time.

1 Table 1. Apatite fission track ages

Sample No.	Longitude (°E)	Latitude (°N)	Elevation (m)	Grains (<i>N</i>)	ρ_s (10^6cm^{-2})	<i>N_s</i>	U* (ppm)	P(χ^2) (%)	Dispersion (%)	Pooled Age (Ma $\pm 1\sigma$) (%)	MTL $\pm 1\sigma$ (μm) (<i>N</i>)	Dpar (μm)
CD746	101.8693	28.3298	2443	24	2.595	116	7.8	41.09	0	26.9 \pm 1.3	13.49 \pm 1.13 (9)	1.87
CD747	101.8723	28.3273	2351	25	2.283	91	8.6	50.24	0	21.9 \pm 1.9	13.48 \pm 0.51 (9)	1.75
CD748	101.8759	28.3273	2198	24	2.878	80	9.6	44.05	0	18.4 \pm 1.4	13.88 \pm 1.10 (11)	1.85
CD749	101.8773	28.3272	2093	22	2.079	75	9.5	42.59	5	18.5 \pm 1.5	NA	1.99
CD750	101.8781	28.3291	1980	23	2.238	75	9.4	38.66	0	19.7 \pm 1.2	13.62 \pm 0.78 (12)	NA
CD751	101.8803	28.3293	1903	5	1.314	22	29.2	22.84	0	17.9 \pm 1.2	NA	NA
CD752	101.8772	28.3335	1676	24	2.209	112	10.1	55.95	0	16.9 \pm 0.9	13.85 \pm 0.81 (7)	1.84
CD753	101.8774	28.3354	1545	24	2.106	115	9.6	42.94	0	16.9 \pm 1.4	13.89 \pm 0.53 (7)	2.02
CD754	101.8795	28.3364	1455	22	1.700	79	9.1	51.38	0	16.7 \pm 1.4	13.84 \pm 1.07 (14)	1.85

2 Note: *N*=Number of grains dated and Number of track length measured; ρ_s = spontaneous fission-track density; *N_s* = total number of
3 spontaneous fission tracks counted; U*=Mean uranium content of all crystals measured by LA-ICP-MS; P(χ^2) = chi-squared probability can
4 represent a single population of ages for ν where degrees of freedom $\nu = N - 1$; MTL = Mean confined track length

5 Table 2 Apatite (U-Th)/He Result From the Baishagou Vertical Profile

Sample	Grain replicate	Radius (μm)	Mass (μg)	U (ppm)	Th (ppm)	Sm (ppm)	eU (ppm)	Th/U	4He (nmol/g)	FT 238U	FT 235U	FT 232Th	Raw Age (Ma)	Corrected age (Ma)	1σ (Ma)	Average age (Ma)
CD746	Ap1	57.02	3.80	12.46	46.46	171.34	23.38	3.82	1.40	0.749	0.714	0.714	10.94	14.91	0.18	15.16±1.28
	Ap2	72.39	5.15	7.75	26.34	111.61	13.94	3.49	1.01	0.799	0.771	0.771	13.25	16.82	0.19	
	Ap3	61.54	3.24	6.14	21.91	85.75	11.29	3.66	0.70	0.766	0.734	0.734	11.43	15.19	0.18	
	Ap4	56.27	3.03	7.55	26.96	105.46	13.88	3.67	0.76	0.746	0.711	0.711	10.03	13.72	0.18	
CD747	Ap2	60.51	3.14	7.52	19.06	156.40	11.99	2.60	0.81	0.762	0.730	0.730	12.29	16.34	0.18	15.21±1.59
	Ap3	59.19	2.84	7.08	36.29	137.63	15.61	5.26	0.89	0.757	0.724	0.724	10.43	14.09	0.16	
CD749	Ap1	58.25	3.43	7.92	40.62	138.79	17.47	5.26	0.89	0.754	0.720	0.720	9.35	12.69	0.15	14.27±1.33
	Ap2	68.21	3.74	7.98	35.11	127.44	16.23	4.51	1.00	0.787	0.758	0.758	11.27	14.57	0.15	
	Ap3	65.56	5.42	7.39	40.04	148.97	16.80	5.56	0.98	0.779	0.749	0.749	10.64	13.94	0.15	
	Ap4	53.82	3.05	9.23	45.71	150.26	19.97	5.08	1.24	0.735	0.699	0.699	11.38	15.88	0.17	
CD753	Ap1	57.51	4.86	8.71	31.11	141.63	16.02	3.66	1.74	0.751	0.717	0.717	19.88	26.98	0.28	
	Ap3	66.89	4.96	8.28	29.21	134.60	15.15	3.62	0.72	0.784	0.753	0.753	8.71	11.29	0.12	
	Ap4	56.55	5.13	8.58	29.68	133.49	15.55	3.55	1.24	0.747	0.712	0.712	14.54	19.84	0.20	

6 The AHe ages that exceed the corresponding AFT age are seemed outliers and not used for weighted mean age calculation and inverse modeling.

